nature biomedical engineering

Article

https://doi.org/10.1038/s41551-025-01394-9

A wireless device for continuous measurement of brain parenchymal resistance tracks glymphatic function in humans

Received: 5 January 2024

Accepted: 9 April 2025

Paul Dagum[1]✉, **Laurent Giovangrandi**[1], **Swati Rane Levendovszky**[2], **Jake J. Winebaum**[1], **Tarandeep Singh**[1], **Yeilim Cho**[3], **Robert M. Kaplan**[4], **Michael S. Jaffee**[5,6], **Miranda M. Lim**[7,8,9], **Carla Vandeweerd**[10,11] & **Jeffrey J. Iliff**[3,12,13]

Glymphatic function in animal models supports the clearance of brain proteins whose mis-aggregation is implicated in neurodegenerative conditions including Alzheimer's and Parkinson's disease. The measurement of glymphatic function in the human brain has been elusive due to invasive, bespoke and poorly time-resolved existing technologies. Here we describe a non-invasive multimodal device for the continuous measurement of sleep-active changes in parenchymal resistance in humans using repeated electrical impedance spectroscopy measurements in two separate clinical validation studies. Device measurements successfully paralleled sleep-associated changes in extracellular volume that regulate glymphatic function and predicted glymphatic solute exchange measured by contrast-enhanced MRI. We replicate preclinical findings showing that glymphatic function is increased with increasing sleep electroencephalogram (EEG) delta power and is decreased with increasing sleep EEG beta power and heart rate. The present investigational device permits the continuous and time-resolved assessment of parenchymal resistance in naturalistic settings necessary to determine the contribution of glymphatic impairment to risk and progression of Alzheimer's disease and to enable target-engagement studies that modulate glymphatic function in humans.

The glymphatic system is a brain-wide network of perivascular pathways along which the cerebrospinal fluid (CSF) surrounding the brain exchanges with brain interstitial fluid, supporting nutrient distribution and waste clearance (Fig. 1a,b). In animal models, glymphatic function supports the clearance of amyloid β[1,2], tau[3–5] and α-synuclein[6,7], whose mis-aggregation is implicated in the pathogenesis of neurodegenerative conditions including Alzheimer's and Parkinson's disease. Glymphatic function is further postulated to be a mechanism for volume transmission of the neurotransmitters acetylcholine, serotonin and norepinephrine, and of neurohormones regulating brain–body homeostasis[8]. While this system is foundational to brain health and disease, measurement of glymphatic function in the human brain, principally by magnetic resonance imaging (MRI), is conducted in only a handful of academic neuroimaging centres[9]. Without a consistent, reproducible and accessible way of measuring this important neurobiology in humans, the promise of developing therapeutic interventions that target glymphatic function to treat and prevent neurological and psychiatric diseases remains elusive.

A full list of affiliations appears at the end of the paper. ✉e-mail: paul@appliedcognition.com

Studies in rodents have demonstrated that glymphatic function is more rapid during sleep compared with the awake state[2,10]. During periods of wakefulness, the interstitial space is narrow and tortuous, forming a high-resistance pathway that suppresses glymphatic flow, while during sleep, fluid shifts from the intracellular compartment into the extracellular (interstitial) space, widening these pathways and enhancing glymphatic function by ~60% (Fig. 1c,d). Measuring glymphatic function across a range of physiological conditions in mice demonstrated that faster glymphatic exchange is associated with increased electroencephalogram (EEG) delta band power, decreased EEG beta power and reduced heart rate[11]. Studies using contrast-enhanced (CE)-MRI to measure solute exchange between the CSF and brain interstitial compartments in human participants have confirmed more rapid glymphatic function during sleep[12], although the poor temporal resolution of this approach[13–15] has not permitted the relationship between EEG or cardiovascular features and glymphatic function to be defined in the human brain.

Electrical impedance spectroscopy (EIS) is widely used in medicine for body composition analysis and for monitoring cellular changes in settings including tumours and oedema[16–19]. When alternating current is injected into tissue, at low frequencies, the voltage drop depends primarily on the resistive pathway of the extracellular (interstitial) fluid, while at high frequencies, cell membranes behave like capacitors allowing current to also pass relatively freely through the intracellular space (Fig. 1c–e). This frequency dependence is the β-dielectric dispersion of the underlying tissue, and its repeated measurement permits the detection of shifts in the extracellular and intracellular distribution of water within tissue[17,20].

We propose that the biophysics of EIS can be leveraged to measure the fluid shift that occurs with changes in sleep-active glymphatic function. Because intracranial volume is constant, any change in this frequency dependence across repeated EIS measures reflects changes in the resistance of the extracellular space, which is inversely proportional to the extracellular fluid volume (Fig. 1c–e). Within the brain, the extracellular compartment includes the brain interstitial space (~16% of total volume) and a combination of CSF (~10%) and blood plasma (~6%)[21]. Small diurnal fluctuations occur in blood volume and in the CSF compartments, but these changes are small and offset one another across physiological states[22,23]. In contrast, sleep–wake differences in glymphatic function are associated with much larger shifts in the intracellular and particularly interstitial volumes[2]. Thus, sleep–wake changes in EIS measures will be sensitized to changes in brain intracellular and interstitial volume, and EIS-based measures of parenchymal resistance (R_P) may represent an approach to track a key determinant of sleep-active glymphatic function.

We developed a wearable investigational device (Fig. 2a–f) that overcomes several technical challenges surrounding the implementation of EIS as a measure of parenchymal resistance. To define the dynamic relationship between R_P, sleep EEG features and cardiovascular parameters through the course of an overnight period, EIS measurements must be made with high accuracy and temporal resolution. The investigational device performs measurements at frequencies between 1 kHz and 256 kHz and has a ~3% measurement error in R_P (Supplementary 4), enabling it to detect small changes in dispersion between repeated measures. It is important to ensure that device measurements are not affected by changes in electrode impedances that can occur over time, including those caused by the effects of motion on the electrode–skin interface. A non-traditional four-electrode impedance configuration was used with multiple excitation and sense configurations in combination with low-impedance, non-polarizable electrodes. This ensured high-fidelity measurements including at low frequencies due to the reduced sensitivity to motion artefacts, low noise and stability of the skin–gel–electrode interface. A signal processing approach enabled identification of signal from noise using the real and imaginary parts of the impedance to establish whether the measured response is related to the excitation signal or has been distorted by artefact. The device further integrated shielded cables to reduce effects of electromagnetic interferences, both external and internal to the device, and the design minimized stray capacitances affecting higher frequencies. The device is described in more detail in Methods and Supplementary Information including Supplementary Figs. 2 and 3 and Tables 7–12.

Glymphatic flow is determined by the motive force driving CSF along the perivascular spaces (PVS) into the interstitial compartment and the extracellular resistance to this flow. The motive forces driving CSF along the PVSs and into the interstitial spaces of the brain parenchyma include vasomotor oscillations related to the cardiac cycle and low-frequency vasomotion, as well as synchronous neural activity[24–29]. The resistance to glymphatic flow comprises the upstream PVS resistance and the resistance within the brain interstitial space. The PVS resistance varies with vasomotor function, which alters the cross-sectional area of this space. The resistance of the interstitial space is dynamically regulated across conditions of sleep, wake and different anaesthetic settings[2,30]. The investigational device measures transcranial parenchymal resistance with high temporal resolution, which is sensitive to changes in global intracellular–interstitial fluid shifts. This measure of parenchymal resistance (R_P) is expected to track brain interstitial resistance to glymphatic flow. In the present study, we conducted two trials in healthy older participants to test whether brain parenchymal resistance declines with sleep, and whether as in rodents[2,11,27], parenchymal resistance, sleep-related changes in EEG features and heart rate (HR) regulate glymphatic function in the human brain.

Results

Data were acquired using the investigational medical device developed by Applied Cognition[31,32]. Transcranial impedance dispersion was estimated from each EIS measure using a dielectric relaxation model. In addition to EIS measurements, the device measures EEG, photoplethysmogram (PPG), impedance plethysmogram (IPG) and head motion (Fig. 2a–f). We propose that the change in transcranial impedance dispersion, which we will henceforth term parenchymal resistance R_P ($R_P = R_0 - R_\infty$), reflects shifts in brain intracellular and interstitial compartment fluid volumes that underlie changes in glymphatic function (Fig. 1c–e). Supplementary Information 3 contains an intuitive justification of the physiological connection between EIS change and changes in glymphatic function. To test this, we evaluated whether R_P measured with this device in human participants aligned with the central features of glymphatic function described in rodent models[2,11,27].

Study design

We conducted two clinical studies (denoted as ‘Benchmarking Study’ and ‘Replication Study’) to validate the performance of the device’s R_P measure as a surrogate of glymphatic flow resistance during sleep and wake (Fig. 3, top). Both studies were cross-over trials where participants wearing the investigational device were subjected to one night of natural sleep and one night spent awake, separated by two or more weeks. The Benchmarking Study was conducted in The Villages community, an active-lifestyle senior living community in Central Florida where the University of Florida maintains a satellite academic research centre, The University of Florida Health Precision Health Research Center (UF Health PHRC). The Benchmarking Study was designed to define the effect of sleep on overnight R_P measurements, as well as the relationship between R_P and glymphatic function. It included overnight device recordings, overnight gold-standard polysomnography (PSG) and morning CE-MRI following intravenous gadolinium-based contrast agent (GBCA) administration as a measure of glymphatic function. During the morning period, following pre-contrast MRI scanning, GBCA injection and immediate post-contrast MRI scanning (totalling 2.5 h spent awake), participants who were sleep deprived overnight were provided a 1.5 h sleep opportunity before the final MRI scan, while those

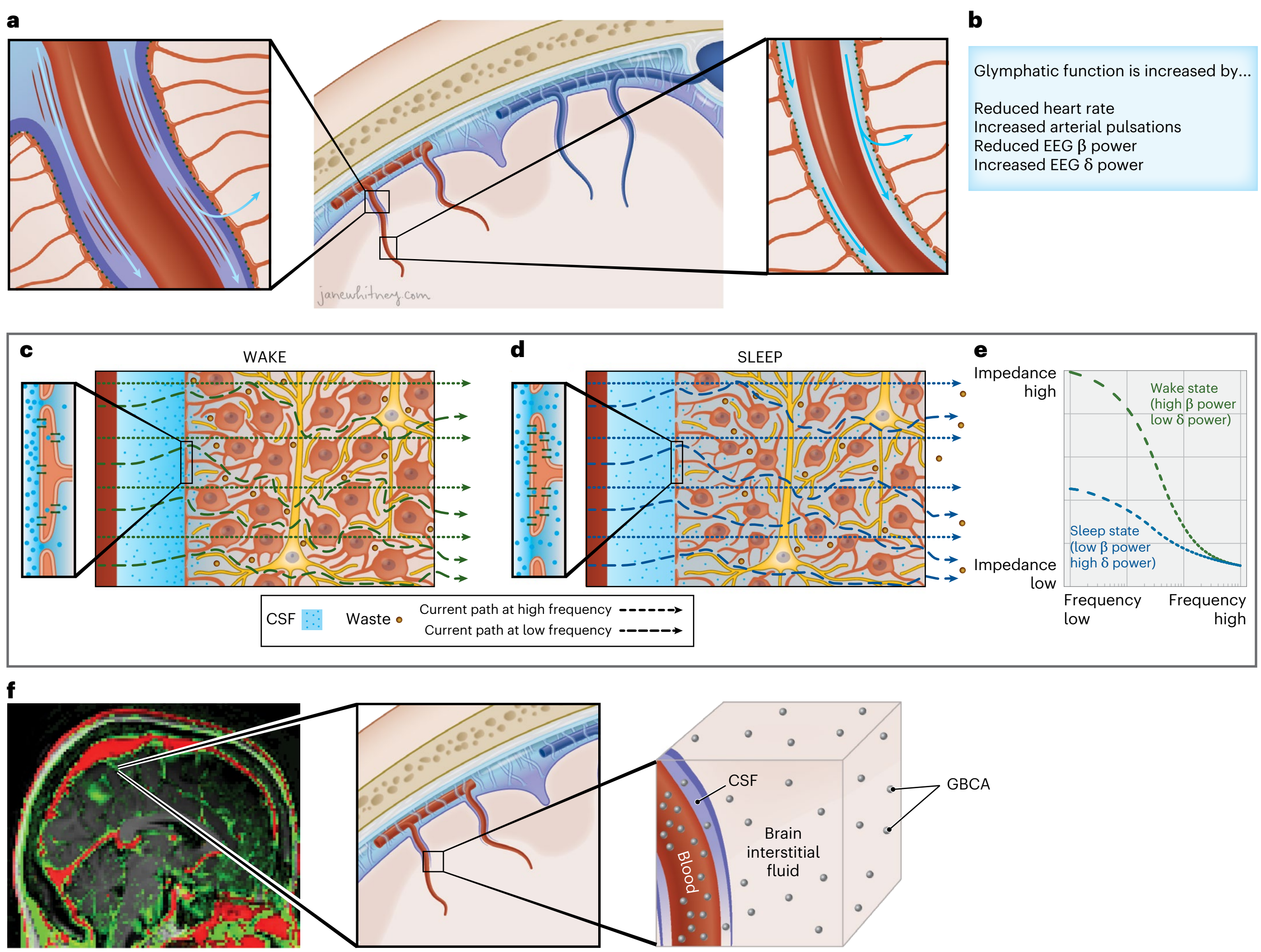

Fig. 1 | Effect of glymphatic function on parenchymal resistance analysed via dynamic impedance spectroscopy. a, Glymphatic function involves the influx of cerebrospinal fluid along perivascular spaces surrounding penetrating arteries (centre). Glymphatic flow is driven by arterial pulsation, vasomotor oscillations and synchronous neural activity (right). Astrocytic endfoot processes create the barrier between the PVS and the brain parenchyma, with gaps allowing CSF to exchange through the brain interstitial space. The arrows represent cerebrospinal fluid flow along the perivascular spaces and into the brain interstitial space. **b**, Data from physiological studies in rodents suggest that glymphatic function is increased in conditions of reduced heart rate, increased vasomotor pulsations, reduced EEG beta power and increased EEG delta power[11]. **c**, The interstitial space is dynamically regulated. Under conditions common to the awake state, it is narrow and tortuous, forming a high-resistance pathway that suppresses glymphatic flow. When alternating current is injected into the brain parenchyma, at low frequencies the current cannot penetrate the cell membranes and its propagation depends primarily on the resistive pathway of the interstitial fluid. At high current frequencies, the current readily penetrates the cell membranes and its propagation depends on the resistance of the total tissue volume. This frequency difference is the β-dielectric dispersion of the underlying tissue. A change in the dielectric dispersion reflects a change in the low-frequency resistance pathway of the interstitial fluid. **d**, In the sleep state, fluid shifts from the intracellular compartment into the interstitial space, enhancing glymphatic function by ~60% in rodent studies[2]. This widening of interstitial pathways reduces the current resistance at low frequencies, which reduces the measured dielectric dispersion. **e**, An impedance–frequency graph shows the change in dielectric dispersion between the two sleep/wake states. The change in parenchymal resistance between these two states is inversely proportional to the relative change in the dielectric dispersion. **f**, Contrast-enhanced MRI following intravenous GBCA injection shows vascular regions that enhance immediately ($t = 30$ min) upon GBCA injection (red), and CSF and brain parenchymal regions that enhance late ($t = 3$ h) after leakage of GBCA first into the CSF and then into the brain interstitium (green). A given MRI voxel includes GBCA within the blood, CSF and brain interstitial fluid compartments. Illustrations: Applied Cognition.

who slept normally overnight were kept awake during the 1.5-h period (Fig. 3, top). We evaluated whether, as predicted from previous rodent studies on the sleep-modulation of glymphatic function[2,11,27], (1) R_P is reduced in sleeping compared with awake participants, (2) reduced R_P is associated with more rapid CSF–brain interstitial solute exchange measured by CE-MRI, (3) R_P is associated with increasing sleep EEG delta power and decreasing sleep EEG beta power and (4) reduced R_P is associated with decreasing heart rate. The Replication Study conducted at the University of Washington did not include overnight PSG or morning CE-MRI and had a primary outcome of confirming the effect of sleep state on device-measured R_P, and secondary outcomes of confirming the associations between R_P and sleep stages, heart rate and EEG spectral band power. As noted in the detailed study description in the Methods section, these studies also evaluated non-contrast MRI measures of glymphatic function, sleep-sensitive changes in cognitive function and sleep-sensitive changes in plasma Alzheimer's disease biomarkers across a range of physiological sleep conditions. Those findings will be reported elsewhere.

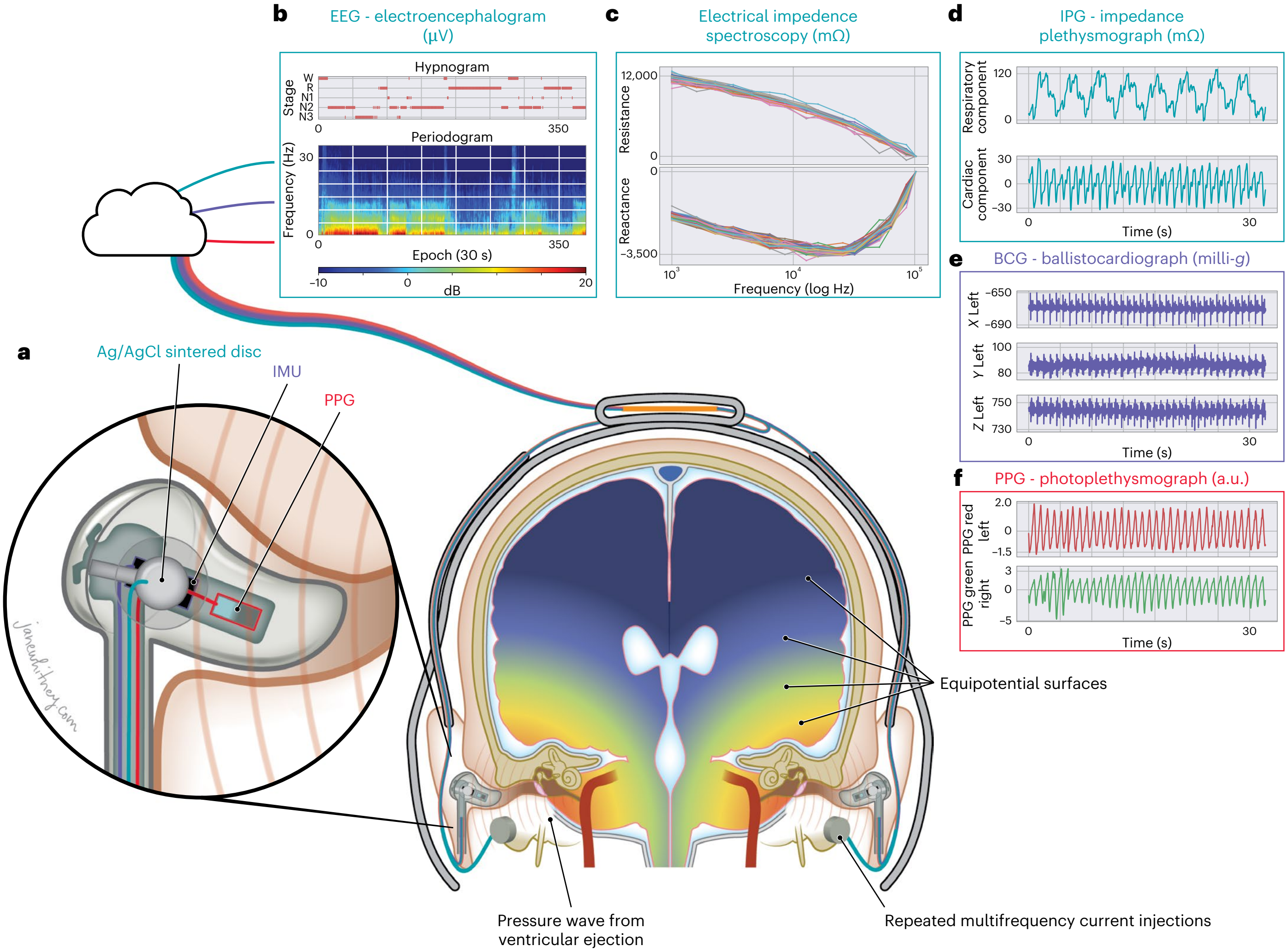

Fig. 2 | Technical schematic of investigational device and its output signals. Data for this study were acquired with a non-invasive multimodal skin-interfaced wireless device for continuous measurement of brain parenchymal resistance using repeated EIS time multiplexed with EEG and cardiovascular measurements. EEG differential measurements were made between the two in-ear electrodes, and a left mastoid was used to drive the common mode. These electrodes were shared with the EIS, and the two measurements were time multiplexed with a pair of analogue multiplexers that decoupled EEG and EIS. The transcranial multifrequency alternating current injections created an electric field through the brain and orthogonal equipotential surfaces. **a**, Each in-ear electronics houses PPG and IMU sensors. **b**, Data from the sensors are stored on the device's FLASH memory and transferred via a USB port to a cloud signal processing pipeline for offline analysis. Data from a participant visit is shown, which includes the device EEG periodogram and hypnogram. **c**, The EIS resistance and reactance frequency plots for this participant reveal an approximate 2,000 mOhm change in the dielectric dispersion during the sleep visit. **d**, The IPG respiratory and cardiac impedance variations are 120 mW and 50 mW, respectively. **e**, Cardiac ejection of blood is detected by the in-ear IMUs in the ballistocardiogram. The J peak of the ballistocardiogram marks the aortic valve opening. **f**, Time delay between the ballistocardiogram and in-ear PPG measures the pulse-transit time (PTT) to the ear. Illustrations: Applied Cognition.

Inclusion and exclusion criteria. All studies were performed between October 2022 and June 2023, and were reviewed and approved by the University of Florida Institutional Review Board (IRB No. 202201364, Benchmarking Study) and Western Institutional Review Board (IRB No. 20225818, Replication Study). The studies have been registered at ClinicalTrials.gov (https://clinicaltrials.gov/study/NCT06222385 and https://clinicaltrials.gov/study/NCT06060054). Written informed consent was obtained from all study participants during a screening visit, before any study activities. Studies were carried out in accordance with the principles of the Belmont Report. The Benchmarking Study enrolled 34 healthy participants 56–66 years of age. The Replication Study enrolled 14 healthy participants 49–63 years of age. Participants were excluded if they had cognitive impairment or clinical depression. Cognitive impairment was assessed using the Montreal Cognitive Assessment[33] (MoCA, 28.1 ± 1.2; range 26, 30) and depression was evaluated using the 15-item Geriatric Depression Scale[34] (GDS, 0.7 ± 1.1; range 0, 4). Participants with a self-reported history of diabetes, hypertension, coronary artery disease, pulmonary disease, neurological disease, depression or anxiety were also excluded from the study, as were participants planning travel to alternate time zones within 2 weeks of study participation. Participant demographics, MoCA and GDS scores are listed for each study and for the combined dataset in Supplementary Table 1.

A Consolidated Standards of Reporting Trials (CONSORT) diagram for the Benchmarking Study and Replication Study is provided in Fig. 3c. Within the Benchmarking Study, the first three participants were removed from analysis because of a design change in the investigational device sensor positions. One participant was unable to complete the first MRI session and withdrew from the study. Of the remaining 30 participants (61.8 ± 2.7 years of age; 14 female, 16 male) who completed the Benchmarking Study, 5 overnight sleep studies and 8 overnight wake studies failed data quality control due to excessive artefacts in

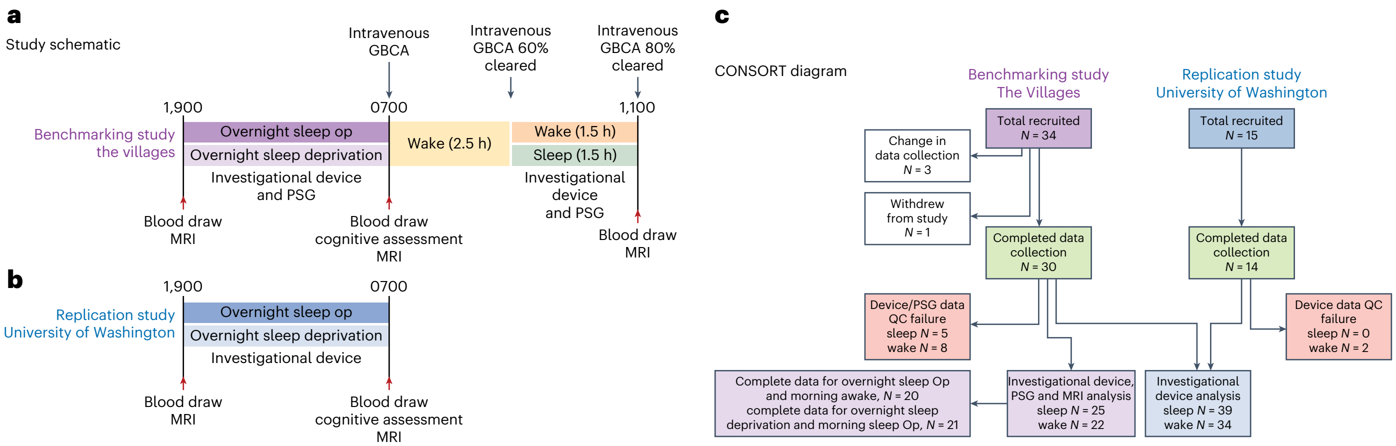

Fig. 3 | Study schematic and CONSORT diagram for Benchmarking Study and Replication Study. a, The Benchmarking Study conducted at The Villages was designed to define the relationship between parenchymal resistance (R_P) and glymphatic function. Reported here are the overnight and morning device recordings, overnight and morning gold-standard PSG, and morning CE-MRI following intravenous GBCA administration as a measure of glymphatic function. Primary and secondary outcome data not reported here included blood analysis of amyloid β and tau levels, cognitive assessment and non-contrast MRI. **b**, The Replication Study conducted at the University of Washington had a primary outcome of confirming the effect of sleep state on device-measured R_P, and secondary outcomes of confirming the associations between R_P and sleep stages, heart rate and EEG spectral band power. The Replication Study also included secondary outcomes on blood analyses for amyloid β and tau levels, cognitive assessment and non-contrast MRI. **c**, The Benchmarking Study enrolled 34 participants of which 30 completed both visits. Three were censored due to changes in device data collection and sensor locations. One withdrew following the first MRI scan. Of the 30 that completed the study, 5 overnight sleep visits and 8 overnight wake visits failed the data quality control (QC) criteria to provide sufficient artefact-free data to yield results. This resulted in 25 sleep and 22 wake device, PSG and MRI complete datasets. Of these, 20 sleep and 21 wake device participants had complete data from both the overnight and morning sleep/wake periods. The Replication Study enrolled 14 participants. All 14 completed the study, of which 2 wake visits failed the data QC criteria and no sleep visit failed. Sleep op, sleep opportunity.

the recordings, leaving 25 overnight sleep studies and 22 overnight wake studies in the Benchmarking Study with complete device, PSG and MRI data. Excessive movement artefacts during the morning recording periods resulted in the exclusion of data from 5 additional morning wake and 1 additional morning sleep opportunity periods, leaving 20 overnight sleep/morning wake and 21 overnight wake/morning sleep opportunity datasets with complete overnight and morning data. All participants enrolled in the Replication Study (55.6 ± 4.6 years of age; 7 female, 7 male) completed the protocol. All overnight sleep data were usable, but 2 overnight wake studies were removed, 1 because of excessive artefact and 1 because of non-compliance with the wake protocol. The higher number of quality control failures in the Benchmarking Study was largely due to the physical challenges caused by simultaneous data acquisition from both PSG and investigational device on the same night. Note that when the investigational device was used in the absence of PSG in the Replication Study, quality control failures were less frequent and restricted to motion artefacts in the awake condition.

Changes in parenchymal resistance with sleep and wake

Study participants underwent one night of normal sleep and one night of sleep deprivation separated by 2–4 weeks. Sleep/wake or wake/sleep visit order was determined by random assignment following informed consent. In the Benchmarking Study, sleep and wake status was confirmed by PSG with anticipated differences in rapid eye movement (REM) and non-REM (NREM: N1, N2, N3) sleep stages observed between sleep and wake conditions. Similar differences were observed in the Replication Study, in which investigational device-based EEG was used to evaluate sleep parameters. EEG was assessed with the investigational device in both the Benchmarking and Replication studies; these measures were used when combining EEG parameters between both studies. Averaged hypnograms showing sleep stage distribution throughout the overnight sleep period for the Benchmarking and Replication studies are shown in Fig. 4a,b (top). The averaged hypnogram for the overnight and morning periods for the Benchmarking Study participants with complete data during both periods is shown in Fig. 4c (left).

During the overnight period, R_P was continuously monitored. The results from the Benchmarking Study are provided in Fig. 4a (bottom), which depicts the mean and standard errors of overnight R_P. Each participant's R_P was normalized to the R_P at onset of the observation period, and linear interpolation was used for missing R_P values within each participant. Compared with the wake condition, overall R_P during sleep was reduced by 8% (wake 1.00 ± 0.06, sleep 0.92 ± 0.06, t-test $P < 0.001$). When evaluated through the course of the overnight period, the R_P during the wake period remained largely constant. In contrast, during the sleep period the mean R_P decreased monotonically, reaching at the end of the sleep period a nadir ~20% lower than at onset or under the awake condition. Similar results were observed in the Replication Study (Fig. 4b, bottom). Within the Benchmarking Study, participants who were sleep deprived overnight received a 1.5 h sleep opportunity in the morning. Over this period, R_P began at a higher value (resulting from overnight sleep deprivation) but declined over the 1.5 h sleep opportunity (Fig. 4c, right). Among participants who slept overnight but were kept awake in the morning, R_P during the morning period began at a low value (resulting from overnight sleep) but increased over the 1.5 h period of wakefulness. These data demonstrate across two study populations that R_P remains constant or increases during periods of waking but declines steadily through periods of sleep.

Association between sleep parameters and glymphatic function

Following the overnight sleep periods, participants in the Benchmarking Study underwent CE-MRI for the assessment of glymphatic function. Beginning at 7:00, participants underwent a pre-contrast T1-weighted MRI scan, received intravenous GBCA (Gadavist, 0.1 mmol kg^{-1}), followed by T1-weighted MRI scans at 7–10 min (T_{10}) and 240 min (T_{240}) post injection. We evaluated contrast enhancement (CE) in 8 regions of interest (ROIs): frontal cortical grey and white matter, parietal cortical grey and white matter, temporal cortical grey and white matter, and occipital grey and white matter. Contrast enhancement at the T_{10} time point primarily reflects GBCA within the blood column, while

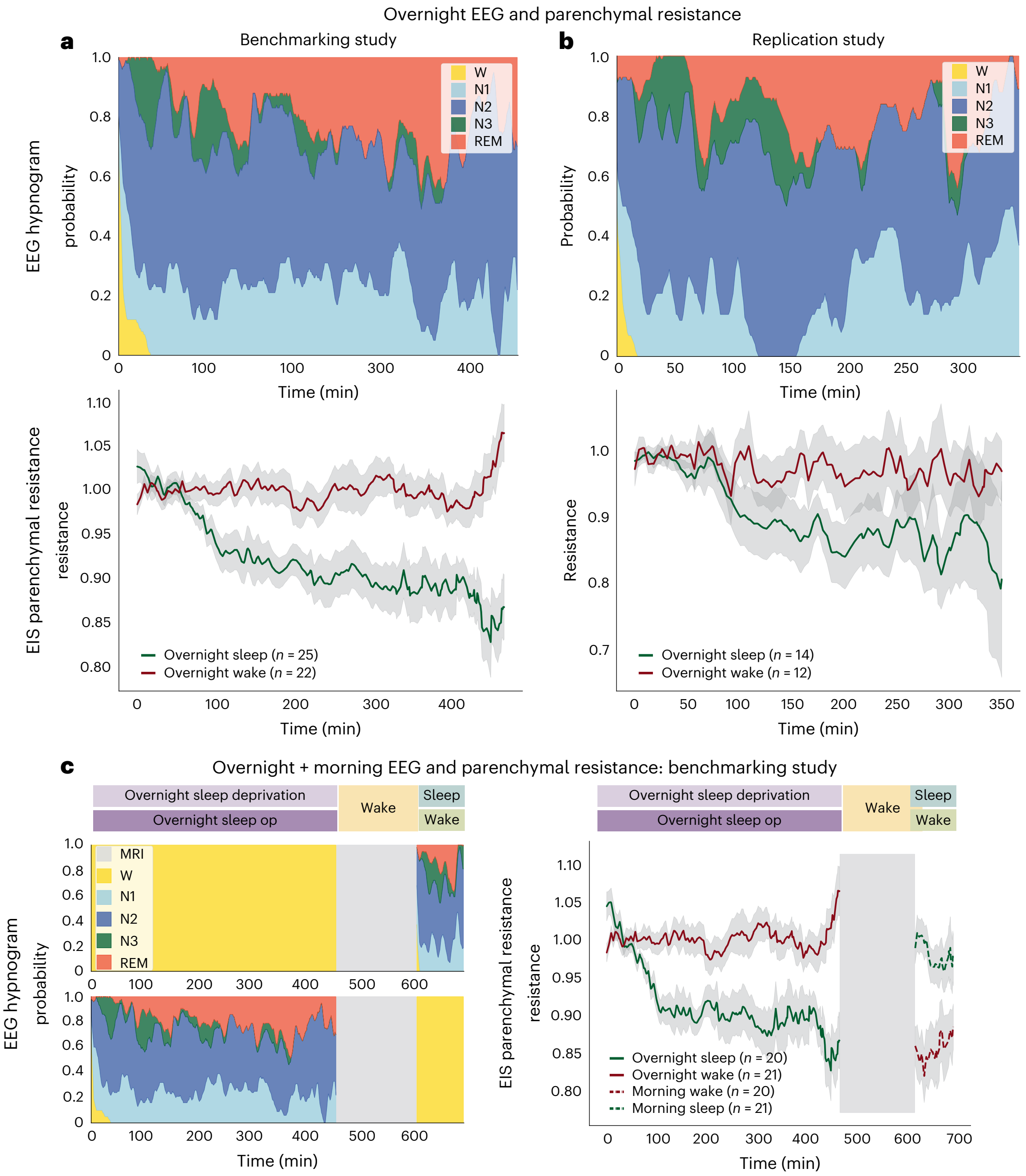

Fig. 4 | Brain parenchymal resistance is reduced during periods of sleep. **a**, Averaged EEG hypnograms from the sleep condition are shown for the overnight period of the Benchmarking Study with WASO excluded in both the hypnograms and sleep R_P (top). Over that period, parenchymal resistance (R_P, bottom) remained constant during the awake state (red) but declined gradually in the sleep state (green). **b**, Similar trends were observed in the Replication Study. **c**, During the morning period of the Benchmarking Study, participants underwent a 1.5 h sleep opportunity or period of wakefulness. Left: averaged EEG hypnograms for the overnight and morning periods. Right: during the morning awake period, R_P increased gradually (dashed red), while it declined gradually during the sleep state (dashed green). Parenchymal resistances R_P shown in **a**, **b** and **c** are the average across the participants after normalizing each participant's R_P measurements by their value at onset of the sleep or wake period. R_P in **c** for morning wake is plotted starting at the ending value of overnight R_P for illustration purposes. Standard error of the mean is shown for each plot in light grey. The combined overnight and morning Benchmarking Study (**c**) includes participants whose overnight and morning data passed quality controls.

enhancement at the T_{240} time point reflects GBCA leakage into the cerebrospinal fluid and into the brain interstitial compartments[14,15]. Glymphatic function was defined by measuring brain parenchymal contrast enhancement, the % change in T1-weighted signal intensity between 10 and 240 min post GBCA injection ($100\% \times (T_{240}-T_{10})/T_0$) within each ROI.

To evaluate different sleep-related contributions to glymphatic function, we developed a general random intercept mixed model with the 8 ROI groups fit to the T_{10}–T_{240} change in brain parenchymal enhancement. Our 'null hypothesis' was that parenchymal contrast, including contrast in the interstitial compartment, was not influenced by sleep variables. Glymphatic function supports the movement of solutes into and out of the brain interstitial compartment, yet brain parenchymal enhancement includes contrast signal from the blood compartment (the initial source of the GBCA) and the CSF compartment (the intermediate space linking the blood and brain interstitium) in addition to the interstitial compartment (Fig. 1f). Thus, we defined the 'null model' to include regressors for vascular and CSF contrast in the mixed model: the T_{10}–T_{240} change in blood signal within the internal carotid artery and the T_{10}–T_{240} change in CSF signal within the cerebral lateral ventricles. We also included the confounding biological variables of age, gender and APOE ε4 status in the null model shown in Supplementary Table 2 (bottom). The analyses of EEG powerbands, heart rate and sleep staging were performed on the overnight sleep period recordings. Pulse plethysmography and EEG were acquired concurrently, and heart rate, EEG powerbands, sleep stage durations (REM; N1, N2, N3 NREM), number of awakenings and wake after sleep onset (WASO) were computed and included independently in the null model (Supplementary Table 2), and likelihood ratio tests used to compare the individual predictor model with the null model. Relative EEG delta, theta, alpha and beta powerbands were each expressed as the overnight mean of the powerband normalized to the average powerband value of the first three sleep epochs. Higher EEG delta power (mean: 19.12; 95% confidence interval (CI): 5.4819, 32.7599; $P = 0.0072$), lower EEG alpha (mean: −7.28; 95% CI: −12.2638, −2.2935; $P = 0.0052$) and beta (mean: −5.33; 95% CI: −7.7859, −2.8728; $P < 0.001$) power were significantly associated with greater contrast enhancement. We next evaluated EEG-derived sleep stages within individual mixed models. Neither number of awakenings during the sleep period, nor wake after sleep onset were associated with parenchymal contrast enhancement. Lower N1 sleep time was significantly associated with greater parenchymal contrast enhancement (mean: −0.1274; 95% CI: −0.2130, −0.0420; $P = 0.0043$), while N2, N3 and REM sleep time had no significant association with parenchymal enhancement within these individual models (Supplementary Table 2). Thus, within individual mixed models, increased overnight EEG delta band power, reduced alpha and beta band power and reduced time in N1 sleep are each associated with greater glymphatic function, each rejecting the null hypothesis that parenchymal contrast was not influenced by sleep variables (Supplementary Table 2).

Parenchymal resistance associates with glymphatic function

The device R_P values were computed repeatedly throughout the overnight sleep period from each EIS scan. During sleep recordings, the R_P was non-stationary, decreasing throughout the night as shown in Fig. 4a–c. We observed that lower overnight R_P was significantly associated with higher glymphatic contrast enhancement (mean: −38.08; 95% CI: −61.34805, −14.8115; $P = 0.0018$, Supplementary Table 2).

Combined effect of overnight parenchymal resistance, EEG spectral power and heart rate on glymphatic function

We next utilized a comprehensive mixed model to define the contributions of R_P, EEG spectral band power and heart rate to parenchymal contrast enhancement. As in the individual mixed models above, this comprehensive model extended the null model that contains only contrast enhancement in the blood and cerebral ventricles as regressors, and age, APOE4 status and gender as confounding biological variables. We evaluated the relative delta, theta and beta powerbands, omitting the alpha powerband to avoid multicollinearity in the model. We subjected the model to a backward elimination (BE) algorithm with a Wald's P-value threshold of 0.05. Table 1 provides the full outputs of the analyses for each of the four intervention periods of overnight sleep opportunity, morning sleep opportunity, overnight sleep deprivation and morning awake of the study (Fig. 3, top).

In reference to the models selected by backward elimination shown in Table 1, as expected, both blood and ventricular CSF contrast enhancement were strongly associated with parenchymal enhancement following the overnight sleep opportunity (blood mean: 8.89; 95% CI: 3.62, 14.16; $P = 0.001$; CSF mean: 170.45; 95% CI: 143.86, 197.04; $P < 0.001$) and overnight sleep deprivation (blood mean: 13.09; 95% CI: 7.09, 19.10; $P < 0.001$; CSF mean: 162.36; 95% CI: 129.54, 195.19; $P < 0.001$). For the overnight sleep opportunity, lower heart rate (mean: −54.48; 95% CI: −79.51, −29.45; $P < 0.001$) and lower R_P (mean: −52.55; 95% CI: −74.76, −33.33; $P < 0.001$) predicted greater contrast enhancement. Reduced EEG beta power predicted greater parenchymal enhancement (mean: −6.29; 95% CI: −8.54, −4.05; $P < 0.001$), while neither delta nor theta power exhibited significant associations within the multivariate model. In the overnight sleep deprivation condition, reduced EEG delta power (mean: −20.77; 95% CI: −34.34, −7.20; $P = 0.004$) and increased theta power (mean: 7.89; 95% CI: 1.13, 14.64; $P = 0.026$) predicted greater parenchymal enhancement, while neither beta power, heart rate nor R_P showed significant associations within the multivariate model.

Combined effects of morning parenchymal resistance, EEG spectral power and heart rate on glymphatic function

As shown in the study schematic (Fig. 3, top), between 7:10 and 9:30 (140 min post injection, T_{140}), participants underwent MRI scanning followed by instrumentation with the investigational device and PSG for the morning sleep opportunity or awake intervention. Because the mean terminal half-life of intravenous GBCA in adults with normal renal function is 109 min[35], the post-injection blood contrast during the morning recordings was 60% cleared by T_{140} and 80% cleared by T_{240}. Glymphatic function in the period between T_{140} and T_{240} would therefore dilute existing parenchymal contrast, with CSF having 60% to 80% lower contrast concentration, a process analogous to 'clearance' of interstitial contrast. Thus, we would expect that an increase in glymphatic function during the period between T_{140} and T_{240} would be reflected as reduced parenchymal contrast enhancement at T_{240} (Supplementary Fig. 1).

In reference to the models selected by backward elimination in Table 1, once again both blood and ventricular CSF contrast enhancement were strongly associated with parenchymal enhancement following the morning sleep opportunity (blood mean: 11.73; 95% CI: 7.89, 15.57; $P < 0.001$; CSF mean: 145.25; 95% CI: 125.08, 165.42; $P < 0.001$) and awake intervention (blood mean: 9.83; 95% CI: 5.37, 14.29; $P < 0.001$; CSF mean: 232.52; 95% CI: 210.27, 254.77; $P < 0.001$). During the morning sleep opportunity, R_P begins to decrease (Fig. 4c). Higher EEG delta power (mean: −35.94; 95% CI: −44.10, −27.78; $P < 0.001$) and lower R_P (mean: 55.35; 95% CI: 33.01, 77.70; $P < 0.001$) predicted reduced parenchymal enhancement (greater contrast clearance).

During the morning awake period, R_P increases from its overnight sleep ending level (Fig. 4c). During this intervention, higher EEG delta power (mean: −20.98; 95% CI: −30.19, −11.77; $P < 0.001$), theta power (mean: −15.27; 95% CI: −19.51, −11.03; $P < 0.001$) and beta power (mean: −21.38; 95% CI: −24.34, −18.43; $P < 0.001$) predicted greater contrast clearance as did lower heart rate (mean: 235.70; 95% CI: 201.64, 269.76; $P < 0.001$) and lower R_P (mean: 29.38; 95% CI: 5.63, 53.13; $P < 0.021$). These findings are similar to those observed for the morning sleep opportunity and consistent with the explanation that an increase in glymphatic influx of CSF during this period dilutes the interstitial space fluid (ISF) contrast concentration and reduces the T_{240} MRI signal intensity.

We used bootstrap analysis of the backward elimination algorithm for stability investigations on the impact of variable selection on bias and variance of the regression coefficient and bootstrap inclusion frequencies. We estimated the multivariate model using the backward elimination algorithm on 500 bootstrap data replicates with replacement for each intervention period (Table 1). The bootstrap inclusion frequency represents the percent of the 500 backward elimination models that retained each variable, while the bootstrap median is the median estimate for that variable. The relative conditional bias quantified the omitted variable selection bias of each variable from inclusion/non-inclusion of other variables from the full model. In the overnight sleep opportunity, in addition to vascular and CSF contrast enhancement (each with an inclusion frequency of 100%), R_P (70.2%), EEG beta power (98.4%) and heart rate (93.0%) had high bootstrap inclusion frequencies and bootstrap median estimates comparable to the selected model estimates. Device-measured R_P and ventricular contrast enhancement had the lowest relative conditional bias, and therefore their predictions of parenchymal contrast uptake were least

Table 1 | Multivariate models of brain parenchymal contrast enhancement using R_{p}, HR and EEG powerband predictors

Predictor period	Full model				Selected model				Bootstrap analysis		
	Fixed-effect predictors	Estimate	CI	*P*	Estimate	CI	*P*	Bootstrap inclusion frequency (%)	RMSD ratio	Relative conditional bias (%)	Bootstrap median
Overnight sleep opportunity	Blood CE	10.57	(4.89, 16.25)	**<0.001**	8.89	(3.62, 14.16)	0.001	100	1.00	−11.89	9.22
	CSF CE	169.37	(141.53, 197.22)	**<0.001**	170.45	(143.86, 197.04)	<0.001	100	0.96	0.70	171.06
	Age	0.50	(−0.03, 1.04)	0.071	–	–	–	29.8	1.40	63.40	0
	Male sex	−6.10	(−9.89, −2.31)	**0.002**	−2.98	(−5.63, −0.34)	0.030	61.0	1.10	−29.97	−3.19
	APOE ε4	5.13	(1.89, 8.37)	**0.003**	4.29	(1.13, 7.46)	0.010	71.2	0.84	−1.90	4.08
	R_{P}	−55.47	(−77.74, −33.20)	**<0.001**	−52.55	(−74.76, −30.33)	<0.001	70.2	1.03	2.38	−49.70
	Delta power	12.69	(−1.93, 27.32)	0.098	–	–	–	28.0	1.25	−15.65	0
	Theta power	−8.69	(−18.01, 0.63)	0.075	–	–	–	18.4	1.77	−9.60	0
	Beta power	−5.21	(−8.11, −2.32)	**0.001**	−6.29	(−8.54, −4.05)	<0.001	98.4	1.03	14.11	−5.96
	Heart rate	−81.28	(−112.92, −49.63)	**<0.001**	−54.48	(−79.51, −29.45)	<0.001	93.0	1.63	−26.68	−57.59
Morning sleep opportunity	Blood CE	10.76	6.24, 15.29	**<0.001**	11.73	(7.89, 15.57)	**<0.001**	99.6	0.89	3.26	11.30
	CSF CE	154.87	125.96,183.78	**<0.001**	145.25	(125.08, 165.42)	**<0.001**	100.0	1.02	−0.58	151.27
	Age	−1.38	−1.95, −0.81	**<0.001**	−1.26	(−1.74, −0.79)	**<0.001**	99.6	1.05	−1.70	−1.33
	Male sex	−0.36	−2.75, 2.02	0.771	–	–	–	13.6	2.38	425.36	0
	APOE ε4	−2.89	−6.31, 0.53	0.109	−3.94	(−6.74, −1.15)	**0.007**	53.6	1.17	58.42	−3.17
	R_{P}	56.58	32.87, 80.29	**<0.001**	55.35	(33.01, 77.70)	**<0.001**	98.6	1.03	−5.03	53.67
	Delta power	−39.36	−51.30, −27.42	**<0.001**	−35.94	(−44.10, −27.78)	**<0.001**	100.0	1.03	−2.48	−37.30
	Theta power	9.01	−6.18, 24.20	0.259	–	–	–	40.0	1.26	74.24	0
	Beta power	−2.68	−12.06, 6.70	0.585	–	–	–	24.0	1.85	190.46	0
	Heart rate	72.92	44.23, 101.62	**<0.001**	77.55	(49.74, 105.35)	**<0.001**	100.0	0.88	5.61	77.21
Overnight sleep deprivation	Blood CE	7.42	−0.407, 15.25	0.076	13.09	(7.09, 19.10)	**<0.001**	56.6	1.59	72.95	8.57
	CSF CE	199.82	152.77, 246.87	**<0.001**	162.36	(129.54, 195.19)	**<0.001**	100.0	1.81	−0.67	193.14
	Age	0.06	−0.60, 0.72	0.871	–	–	–	4.0	2.01	−118.25	0.
	Male sex	−6.53	−10.37, −2.70	**0.002**	−4.81	(−8.05, −1.57)	**0.005**	90.8	0.96	1.08	−6.23
	APOE ε4	6.17	−0.71, 13.05	0.093	–	–	–	58.4	1.60	60.69	6.40
	R_{P}	12.37	−31.98, 56.71	0.600	–	–	–	8.8	1.31	199.07	0
	Delta power	−31.79	−54.44, −9.13	**0.009**	−20.77	(−34.34, −7.20)	**0.004**	85.4	1.24	12.63	−30.78
	Theta power	19.96	7.38, 32.53	**0.003**	7.89	(1.13, 14.64)	**0.026**	83.8	1.45	7.75	19.85
	Beta power	−17.30	−32.72, −1.89	**0.036**	–	–	–	62.0	1.26	42.29	−17.71
	Heart rate	−25.01	−63.14, 13.11	0.218	–	–	–	44.2	1.75	97.16	0

Table 1 (continued) | Multivariate models of brain parenchymal contrast enhancement using R_P, HR and EEG powerband predictors

Predictor period	Full model				Selected model				Bootstrap analysis		
	Fixed-effect predictors	Estimate	CI	*P*	Estimate	CI	*P*	Bootstrap inclusion frequency (%)	RMSD ratio	Relative conditional bias (%)	Bootstrap median
Morning awake	Blood CE	10.58	5.67, 15.49	**<0.001**	9.83	(5.37, 14.29)	**<0.001**	98.0	0.86	−5.59	9.91
	CSF CE	232.82	210.603, 255.04	**<0.001**	232.52	(210.27, 254.77)	**<0.001**	100.0	1.07	0.84	233.00
	Age	−0.88	−1.72, −0.04	0.049	−0.72	(−1.43, −0.01)	0.057	63.8	1.14	28.44	−0.81
	Male sex	0.96	−1.69, 3.61	0.495	–	–	–	20.2	2.18	223.65	0
	APOE ε4	11.02	8.30,13.74	**<0.001**	10.54	(8.16, 12.92)	**<0.001**	100.0	1.63	−2.35	10.62
	R_P	25.30	−0.93, 51.53	0.071	29.38	(5.63, 53.13)	**0.021**	64.0	1.15	51.96	30.70
	Delta power	−22.53	−32.67, −12.39	**<0.001**	−20.98	(−30.19, −11.77)	**<0.001**	98.6	1.38	−5.75	−21.33
	Theta power	−15.37	−19.62, −11.134	**<0.001**	−15.27	(−19.51, −11.03)	**<0.001**	100.0	1.15	−2.22	−15.00
	Beta power	−21.09	−24.15, −18.04	**<0.001**	−21.38	(−24.34, −18.43)	**<0.001**	100.0	1.13	0.73	−21.42
	Heart rate	230.91	194.43, 267.38	**<0.001**	235.70	(201.64, 269.76)	**<0.001**	100.0	1.19	0.74	234.67

σ^2, within ROI variability; $\tau_{00\,\mathrm{ROI}}$, interROI variability. Wald *t*-test two-sided *P* values are reported for fixed-effect predictor estimates without correction for multiple comparisons. Shaded cells demark the 'null model' that includes blood CE, CSF CE and potential biological confounders.

affected by inclusion of the other variables. Findings in the morning sleep opportunity also showed high inclusion frequencies of the variables retained in the backward elimination algorithm on the full dataset and bootstrap median estimates comparable to the selected model estimates, with vascular contrast enhancement (99.6%), CSF contrast enhancement (100%), R_P (98.6%), EEG delta power (100%) and heart rate (100%). These regressors also had low relative conditional bias. These analyses suggest high model stability to perturbations of the dataset[36].

Lastly, we computed the percent of the residual variance of the null model that was explained by including EEG powerband, heart rate and R_P regressors for each intervention, and computed the likelihood ratio test between the null model and the intervention models. For the overnight sleep and sleep deprivation interventions, 24.5% and 12.7% of the residual null model variance were respectively explained by including these regressors. The null hypothesis that parenchymal contrast enhancement is not influenced by these variables was rejected for the overnight sleep model (likelihood ratio 52.6, $P < 0.001$) and the sleep deprivation model (likelihood ratio 14.1, $P = 0.015$). Including the regressors in morning sleep and awake models explained 38.3% and 74.8% of the residual null model variance, respectively. The null hypothesis that the parenchymal contrast enhancement is not influenced by these variables during the morning sleep (likelihood ratio 79.5, $P < 0.001$) and awake condition (likelihood ratio 149.6, $P < 0.001$) were also both rejected.

Combined effects of parenchymal resistance and sleep stages on glymphatic function

We developed a second comprehensive mixed model to define the relationship among R_P, sleep stages, heart rate and parenchymal contrast enhancement. As above, this comprehensive model extended the null model that contained contrast enhancement in the blood and cerebral ventricles as regressors, and age, APOE4 status and gender as confounding biological variables. We evaluated WASO time and time in N1, N2, N3 and REM sleep stages. Supplementary Table 3 provides the model output for the overnight sleep opportunity (top) and the morning sleep opportunity (bottom). In the overnight sleep opportunity model selected by backward elimination, as before, lower R_P was significantly associated with greater parenchymal contrast enhancement (mean: −67.17; 95% CI: −87.78, −46.56; $P < 0.001$). In this model, more time in REM sleep (mean: 0.16; 95% CI: 0.09, 0.23; $P < 0.001$) and less time in N1 (mean: −0.32; 95% CI: −0.43, −0.21; $P < 0.001$), N2 (mean: −0.10; 95% CI: −0.15, −0.06; $P < 0.001$), N3 (mean: −0.07; 95% CI: −0.12, 0.02; $P = 0.007$) sleep and WASO (mean: −0.07; 95% CI: −0.12, −0.02; $P = 0.006$) were each associated with greater contrast enhancement. Bootstrap analysis showed that blood and CSF contrast enhancement (each with an inclusion frequency of 100%), as well as R_P (100%), REM sleep time (99.0%), N1 sleep time (98.8%) and N2 sleep time (98.0%) were the most stable elements of the model relating sleep stages to parenchymal glymphatic function, while the root mean square deviation (RMSD) ratio for N2 sleep time, N3 sleep time and WASO showed substantial variance deflation following backward elimination (Supplementary Table 3) that is associated with weak or noise predictors.

In the morning sleep opportunity model selected by backward elimination, lower R_P was significantly associated with greater parenchymal contrast clearance (mean: 34.42; 95% CI: 5.25, 63.59; $P = 0.025$), similar to the EEG band power model for this intervention. In this model, less time in REM sleep (mean: 0.41; 95% CI: 0.20, 0.62; $P < 0.001$) and more time in N1 (mean: −0.26; 95% CI: −0.50, −0.02; $P = 0.04$) and N3 (mean: −0.17; 95% CI: −0.33, −0.021; $P = 0.031$) were associated with less contrast enhancement, or greater contrast clearance. N3 sleep did not survive bootstrap analysis, while R_P, REM and N1 sleep had inclusion frequencies of 65.4%, 88.2% and 61.6%, respectively (Supplementary Table 3).

Effects of sleep stages on brain parenchymal resistance

To understand whether sleep stages had a differential effect on the overnight change in R_P, we computed the mean of the first-order differences ΔR_P for each sleep stage for the Benchmarking and Replication studies separately and combined (Fig. 5). The mean ΔR_P was negative and largest for N2, N3 and REM sleep stages, reaching significance when the values for both studies where pooled together. This suggests that R_P in Fig. 4a–c decreases during N2, N3 and REM sleep.

Effects of large changes in EEG spectral power on brain parenchymal resistance

To define the relationships between sleep EEG powerbands, heart rate and R_P, we modelled the relationship between the first-order difference ΔR_P and the difference in spectral band power (Δdelta, Δtheta, Δalpha, Δbeta) and changes in heart rate ΔHR during NREM, REM and wake (Table 2). We utilized threshold regression to model the relationships between ΔR_P and large changes in (Δ) band power or heart rate. A custom estimation procedure described in Supplementary Information was used to jointly estimate the threshold regression for the full positive and negative ranges of Δ band power and ΔHR. The full output of the threshold regression models is provided for the combined study data in Table 2. In both REM and NREM sleep, a large increase in Δdelta was significantly associated with a decrease in ΔR_P (Fig. 6a). In contrast during REM and NREM sleep, a large increase in Δbeta was significantly associated with an increase in ΔR_P. The threshold models for the significant estimated effects of Δ band power on ΔR_P are plotted in Fig. 6b. The full output of the threshold regression model is provided for each site individually in Supplementary Table 4. Because the variables were standardized before model estimation, the regression estimates in Table 2 and Supplementary Table 4 can be interpreted as standardized effect sizes. Note that because of the slope ratio r, changes that exceed the positive change point t_p have effect sizes given by the regression estimate multiplied by the slope ratio. The positive and negative thresholds are in units of standard deviation.

The asymmetric effect of EEG band power changes on R_P shown in Fig. 5 accounts for the progressive decline in R_P that occurs through the course of the overnight sleep period, shown in Fig. 4a–c. In the overnight wake state, Δbeta had a significant but small effect on ΔR_P. ΔHR in NREM and wake had a small effect on ΔR_P and a larger but non-significant effect in REM. The threshold model findings in Table 2 and plots in Fig. 6a demonstrate that large changes in spectral band power are needed to alter R_P. Because such large changes in EEG powerbands and HR occur at sleep stage transitions, we explored the associations between Δdelta and Δbeta and ΔR_P at NREM–REM and REM–NREM transitions, and at sleep–wake and wake–sleep transitions. Table 2 provides the full model output on sleep stage transitions for data pooled from both study sites, while the significant estimated effects of Δdelta and Δbeta on ΔR_P are plotted in Fig. 6c. The full output of the threshold regression model on sleep stage transitions is provided for each site individually in Supplementary Table 5. During the NREM–REM, wake–sleep and sleep–wake transitions, changes in EEG beta power and not EEG delta power underlie the observed changes in ΔR_P. In contrast, during the REM–NREM transition, changes in EEG delta power and not beta power were associated with changes in ΔR_P. In total, these data show that glymphatic function is enhanced by declining R_P, and that R_P in turn declines with reduced EEG beta power and heart rate, and with increasing EEG delta power.

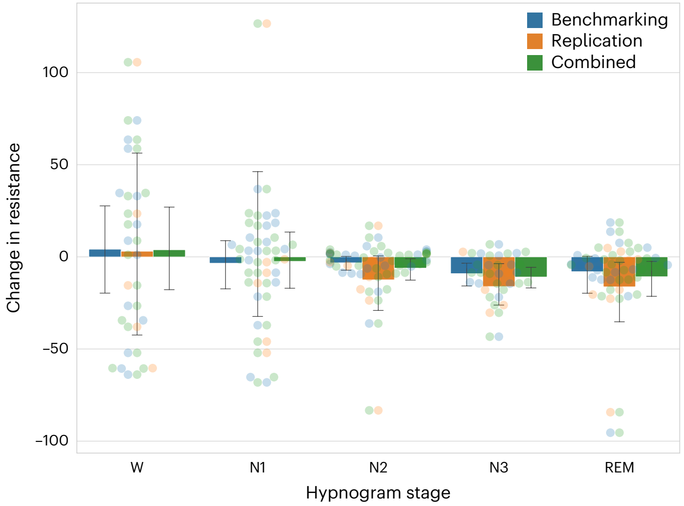

Fig. 5 | Effect of sleep stages on R_P. The mean first-order difference ΔR_P is shown by sleep stage and study for the overnight sleep period with 95% CIs. During N2, N3 and REM sleep, ΔR_P is negative for each study and when combined reaches significance. Benchmarking Study N2 (mean: −3.21; 95% CI: −9.07, −0.33; $P = 0.113$, $n = 22$), N3 (mean: −9.07; 95% CI: −17.04, −3.75; $P = 0.005$, $n = 14$), REM (mean: −8.01; 95% CI: −25.64, −1.18; $P = 0.133$, $n = 18$). Replication Study N2 (mean: −12.46; 95% CI: −34.94, −1.49; $P = 0.115$, $n = 10$), N3 (mean: −16.04; 95% CI: −25.32, −5.32; $P = 0.002$, $n = 5$), REM (mean: −16.24; 95% CI: −42.19, −4.65; $P = 0.065$, $n = 9$). Combined N2 (mean: −6.10; 95% CI: −14.78, −1.71; $P = 0.04$, $n = 32$), N3 (mean: −10.91; 95% CI: −17.35, −5.93; $P < 0.001$, $n = 19$), REM (mean: −10.75; 95% CI: −23.86, −3.91; $P = 0.023$, $n = 27$). Sample sizes for plotted Benchmarking, Replication and Combined Study CIs for W are $n = 13$, 5 and 18, respectively. Sample sizes for plotted Benchmarking, Replication and combined study CIs for N1 are $n = 18$, 7 and 25, respectively. Units of ΔR_P are mΩ. CIs and two-sided P values without adjusting for multiple comparisons were computed using 1,000 bootstrap replications. CIs used the bias-corrected and accelerated (BCa) method, and P values were computed from the Z-score assuming a standard normal distribution.

Discussion

We have described a non-invasive multimodal skin-interfaced wireless device for continuous measurement of brain parenchymal resistance R_P using repeated EIS time multiplexed with EEG and cardiovascular measurements. Through two separate clinical validation studies, we observe that brain R_P declines overnight, paralleling sleep-associated changes in extracellular volume that regulate glymphatic function in rodents[2]. Brain R_P is reduced with increasing sleep EEG delta power and is increased with increasing sleep EEG beta power and heart rate, aligning with the EEG spectral and heart rate determinants of glymphatic function observed in rodents[11]. Lastly, brain R_P alone or in combination with EEG spectral and heart rate data is a robust predictor of glymphatic function, measured by CE-MRI, in the human brain. These findings demonstrate that this investigational device provides a remote, non-invasive and time-resolved measure of parenchymal resistance and sleep EEG suitable for defining this sleep-active glymphatic biology in naturalistic settings.

Several technological advances have enabled this work. We have developed a technique for low-noise EIS measurements using multiple excitation and sense configurations to determine the brain parenchymal impedances accurately. A signal processing approach enabled the segregation of signal and noise, using the Kramers–Kronig relations[37,38] between the real and imaginary parts of the impedance to establish whether the measured response is related to the excitation signal or has been distorted by noise or other artefact. Unlike applications of EIS to neurological conditions such as seizures, tumours or cerebral edema[39–42], the rapid evolution of glymphatic function during sleep and its nightly variability make it suitable for monitoring with longitudinal repeated assessments. Data collected under a variety of scenarios in benchtop testing, agar phantom testing with biological interfaces and in-human testing indicate that this system yields consistent, repeatable results and shows longitudinal stability of the measured impedances.

A key first step in validating any potential measure of glymphatic function is assessing its performance against established, principally contrast-based, measures of glymphatic exchange. Initial studies characterizing glymphatic function in rodents used dynamic in vivo fluorescence-based imaging[1,2,25]. More recent studies in rodents, and recently in human participants, have used CE-MRI following intrathecal GBCA injection[12,13,43,44]. While CE-MRI following intrathecal GBCA injection provides the most direct and well-established approach for assessing glymphatic CSF–interstitial solute exchange in the human

Table 2 | The change in parenchymal resistance resulting from large changes in EEG band power and heart rate occurring during REM sleep, NREM sleep, wake and at NREM–REM and sleep–wake transitions

Study condition	Fixed effects						Threshold model parameters		
	Period	Predictors	Estimate	CI	*P*	d.f.	Positive threshold	Negative threshold	Slope ratio
Overnight sleep op	NREM	Δdelta	−0.28	(−0.50, −0.058)	**0.014**	1,380	1.5	−1.5	0.7
		Δtheta	−0.08	(−0.23, 0.063)	0.265	1,380	1.5	−0.98	0.5
		Δalpha	−0.14	(−0.30, 0.022)	0.091	1,380	1.5	−1.25	0.65
		Δbeta	0.04	(0.0022, 0.080)	**0.039**	1,380	0.18	−1.5	2
		ΔHR	0.10	(−0.0033, 0.19)	0.059	1,115	0.43	−0.43	0.5
	REM	Δdelta	−0.57	(−0.77, −0.37)	**<0.001**	319	1.5	−1.5	2
		Δtheta	−0.41	(−0.70, −0.13)	**0.005**	319	0	−1.5	0.5
		Δalpha	−0.09	(−0.21, 0.041)	0.189	319	1.45	0	2
		Δbeta	0.45	(0.14, 0.77)	**0.006**	319	1.5	−1.3	0.5
		ΔHR	0.31	(−0.057, 0.68)	0.101	271	1.5	−1.15	0.5
	NREM to REM	Δdelta	−0.29	(−0.82, 0.24)	0.293	67	1.5	−1.05	2
		Δbeta	0.77	(0.04, 1.49)	**0.046**	67	0.6	−1.5	0.5
	REM to NREM	Δdelta	−1.50	(−2.35, −0.66)	**0.001**	58	1	−1.5	0.5
		Δbeta	−0.05	(−0.24, 0.14)	0.615	58	0.1	−1.5	1.85
	Sleep to wake	Δdelta	0.03	(−0.34, 0.4)	0.885	66	1.5	−0.3	1.95
		Δbeta	0.73	(0.13, 1.32)	**0.021**	66	0.35	−1.23	0.5
	Wake to sleep	Δdelta	−0.20	(−0.64, 0.25)	0.392	113	0.05	−1.35	0.6
		Δbeta	0.37	(−0.01, 0.76)	0.065	113	1.5	−1.05	2
Overnight sleep deprivation	Wake	Δdelta	−0.06	(−0.15, 0.034)	0.216	1,137	1.5	0	0.5
		Δtheta	−0.07	(−0.17, 0.035)	0.198	1,137	1.4	−1.45	2
		Δalpha	0.06	(−0.030, 0.14)	0.206	1,137	1.15	0	0.73
		Δbeta	0.12	(0.0075, 0.23)	**0.037**	1,137	1.5	−1.43	1.93
		ΔHR	−0.10	(−0.20, −0.011)	**0.029**	1,002	0.25	−0.25	0.5

EEG band power predictor units in percent of total band power; HR predictor units in beats per minute. Wald *t*-test two-sided *P* values are reported for predictor estimates without correction for multiple comparisons. Predictor and parenchymal resistance values in regression models were scaled to zero mean and unit standard deviation with coefficient estimates representing effect size in standard deviations. Positive and negative thresholds are in units of predictor standard deviation. Models included confounding biological variables age, gender and APOE ε4 status.

brain, GBCAs are not FDA approved for intrathecal injection, and this technique remains an off-label use for these agents. Because the present study population of healthy older community dwelling participants lacked clinical indications that would justify the off-label use of intrathecal GBCA for CE-MRI, we chose to employ CE-MRI following intravenous GBCA injection. Recent studies have demonstrated that following intravenous GBCA injection, a small proportion of intravenous GBCA leaks into the CSF compartments, of which a fraction exchanges into cortical grey and white matter[14,15,45]. With this approach, glymphatic function can be defined by assessing GBCA uptake into and clearance out of brain tissue, while controlling for intravenous and CSF levels of GBCA.

We evaluated whether device-based R_{P} measures track with glymphatic function by measuring overnight and morning R_{P}, EEG and the movement of GBCA into brain tissue over a 4-h timeframe. In the analysis, both overnight and morning R_{P} emerged as robust explanatory variables of net contrast movement in a regression model that included CSF and blood contrast levels, EEG neurophysiological parameters, age, gender and APOE e4 confounders. It is important to note that device-based R_{P} measures are acquired with 2-min temporal resolution, whereas CE-MRI captures overall glymphatic function over a 4-h window. This fine temporal resolution enabled translational validation of the physiological drivers of glymphatic function in the human brain. It further revealed that while key events during sleep were necessary to lower parenchymal resistance R_{P}, low R_{P} was sufficient to enhance glymphatic function independent of sleep in the morning period. In addition, it showed that sleep-related changes in R_{P} do not shift with sleep–wake in a stepwise fashion, but rather accumulate through the course of time spent sleeping or awake. These observations are consistent with previous studies in rodents that used real-time iontophoresis to measure sleep-associated increases in brain extracellular volume fraction[2], as these observational studies did not directly test the causal effect of these changes in extracellular volume on glymphatic function, and did not monitor changes in extracellular volume fraction in a time-resolved manner over extended period. Future studies of the determinants of glymphatic function in human sleep will probably further refine existing conceptual models of sleep–wake regulation of glymphatic function.

The physiological mechanisms regulating glymphatic function have been defined almost exclusively through experimental rodent studies[1,2,10,11,25,26,43,46], due in large part to invasiveness and poor temporal resolution of contrast-based measures of glymphatic function[12–15,43]. It is noteworthy that these rodent studies are not all in agreement. While multiple studies have reported more rapid glymphatic exchange under conditions of sleep, or under certain anaesthetic regimes[2,11,30,47–50], two studies[51,52] have reported apparently slower clearance during sleep or under anaesthesia. In the present human clinical studies, we demonstrate within-participant longitudinal declines in brain R_{P} during overnight sleep, but not in awake participants. During morning recovery sleep, we demonstrate within-participant longitudinal declines in brain R_{P}, and during morning wake we observe increases in brain R_{P}.

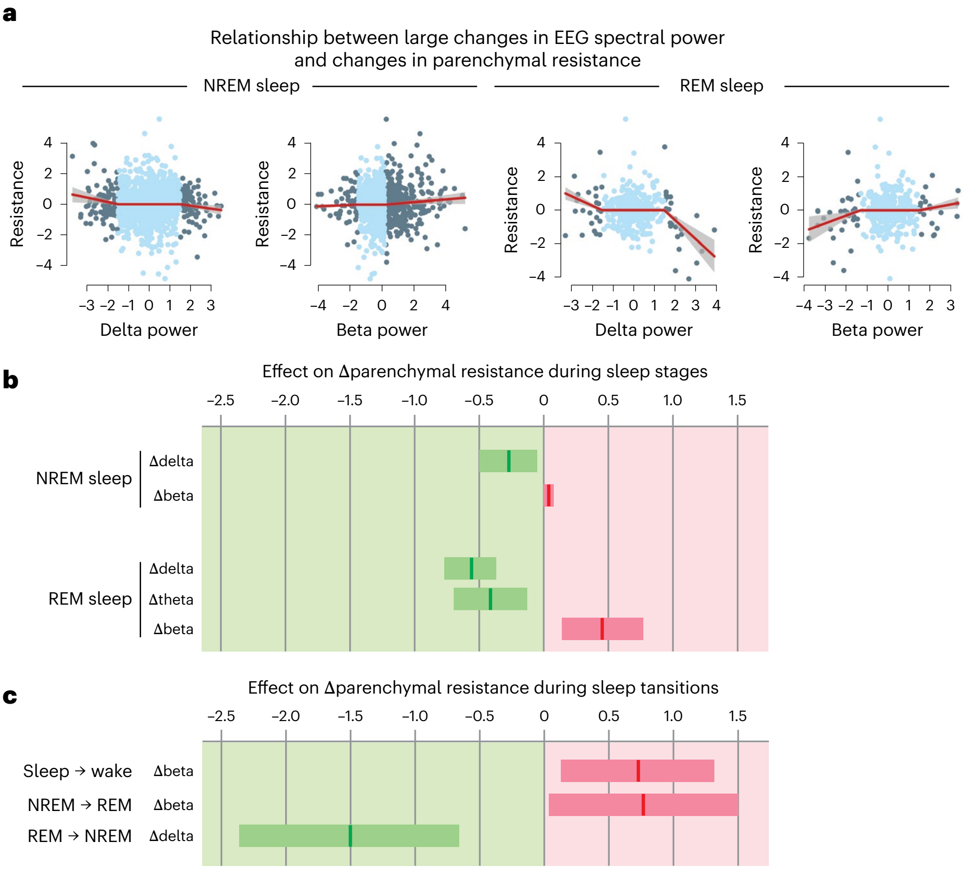

Fig. 6 | Brain parenchymal resistance is increased by large changes in EEG beta power and reduced by large changes in EEG delta power. a, Threshold linear mixed regression model of R_P against EEG delta and beta power for REM and NREM sleep shown with standard error after differencing both R_P and powerband values to make data stationary, standardizing the ΔR_P and Δ powerband values to zero mean and unit standard deviation, and adjusting for site, age, gender, APOE4 and site–age interaction confounders. Units of ΔR_P and Δ powerband are in standard deviations. Data in light blue are inside the change points and data in dark blue are outside the change points. When delta and beta power changes between successive measurements exceed 1.0 to 1.5 stand deviations, we observe significant changes in ΔR_P. **b**, 95% CIs of regression coefficients show that large changes in REM delta, theta and beta, and NREM delta and beta are significant predictors of ΔR_P. For a 1s.d. increase in Δ powerband, an increase (decrease) in ΔR_P is illustrated in red (green) with units along the top in standard deviation of $\Delta R_\mathrm{P.}$ **c**, Large changes in beta and delta powerbands at sleep–wake and NREM–REM transitions show significant effect on ΔR_P consistent with the step change in beta and delta power at these transitions. For a 1s.d. increase in Δ powerband across a sleep–wake or NREM–REM transition, an increase (decrease) in ΔR_P is illustrated in red (green) with units along the top in standard deviation of ΔR_P.

This pattern is consistent with sleep–wake changes in extracellular volume fraction measured and reported in mice[2]. Using overnight PSG followed by CE-MRI in human participants, we confirmed that glymphatic function in the human brain is associated with lower EEG beta power and heart rate, and in a simplified model, with increasing EEG delta power. These findings sustain the physiological findings in mice from ref. 11. More broadly, these human CE-MRI-based imaging studies demonstrate that glymphatic solute exchange is more rapid under conditions of natural sleep, at least in human participants, and that these sleep–wake differences are regulated by sleep-related changes in R_P, heart rate and EEG spectral band power.

Linking changes in R_P with sleep EEG features, we further demonstrate that the investigational device-based measure of R_P exhibits the same dependence on EEG delta power, EEG beta power and heart rate during sleep. Conducting parallel time-resolved sleep EEG and R_P measurements, we observed that rapid changes in R_P occurred at sleep stage transitions between REM and NREM, and between sleep and wake. Transitions between REM and NREM exhibit large changes in EEG delta and beta powerbands, and in HR, consistent with our findings. Large changes in EEG power within a frequency band can occur because of sudden bursts of oscillatory activity within the band's frequency range. In rodents, recent experiments support a role for such synchronized oscillatory activity as a mechanism driving glymphatic flow by creating propagating ionic waves within the brain interstitium[27]. We confirm these physiological drivers of glymphatic function in human participants, within an experimental setting permitting validation against current benchmark CE-MRI-based measures of glymphatic function with well-established preclinical features.

There are clear limitations of both the investigational device and the present study design. CE-MRI following intrathecal GBCA injection provides higher signal-to-noise assessment of glymphatic function than that following intravenous GBCA injection used in the present study; clinical considerations surrounding this off-label use for GBCAs drove this decision. Existing MRI-based measures of glymphatic function remain poorly time resolved but provide excellent cranium-wide anatomical resolution. In contrast, the present investigational device captures a measure of global brain parenchymal resistance with high temporal resolution. While finer anatomical resolution may have value in future iterations of the investigational device, it is important to note that the present design was sufficient to capture sleep–wake changes in glymphatic function and to define neurophysiological drivers of these processes in the human brain. Study methodological limitations include not directly assessing or controlling for changes in the motive forces driving glymphatic transport, including vasomotor oscillations, respiratory and cardiac stroke volume. Additional study methodological limitations include protocol differences between the Benchmarking Study and the Replication Study. The Benchmarking Study included CE-MRI as part of the neuroimaging package and gold-standard PSG concurrent with the device usage, whereas the Replication Study did not include CE-MRI and used the device's single-derivative EEG. Furthermore, the Benchmarking Study enrolled participants 55–65 years old living in Florida, whereas the Replication Study enrolled participants 50–65 years old living on the West Coast. Despite these differences, after adjusting for age, study site and age–site interaction effects, we confirmed that the device's single-derivative EEG showed good agreement with the PSG of the Benchmarking Study. In addition, the pooled analysis and study-specific analyses of R_P, EEG and HR were all in good agreement between studies. The Benchmarking Study was powered to detect a low to moderate correlation between R_P and CE-MRI measures of glymphatic function, which was confirmed. Quality control of the investigational device filtered out measurements that did not satisfy the Kramers–Kronig relations[37,38]. Failed measurements were more common in the Benchmarking Study, particularly during the awake conditions. This is attributable to excessive motion, probably due to the technical challenges associated with conducting concurrent PSG and device-based sleep EEG measures in participants being kept awake by study staff. The low rate of quality-control failures in the Replication Study that did not involve PSG instrumentation supports this conclusion.

The characterization of the glymphatic system in rodents beginning in 2012 has spurred a great deal of interest into its potential mechanistic role linking sleep to cognitive performance, and sleep disruption to a wide range of neurological and psychiatric conditions including Alzheimer's disease, Parkinson's disease, chronic traumatic encephalopathy, stroke, traumatic brain injury, headache and others[53–56]. Preclinical studies have demonstrated that glymphatic function is impaired in the setting of aging[48], sleep disruption[2], cerebrovascular injury[57,58] and traumatic brain injury[3], all risk factors for neurodegenerative conditions including Alzheimer's disease. Experimental impairment of glymphatic function is sufficient to promote the development of the amyloid β[59–61] and tau pathology[3–5] characteristic of Alzheimer's disease. In clinical populations, genetic and histological associations support a link between glymphatic dysfunction and the development of clinical disease[60,62–64]. Yet the technical challenges of real-time dynamic measurements of glymphatic function in human clinical populations have proven a challenging barrier to defining the causal role of glymphatic function and dysfunction in the development of neurological and psychiatric conditions in these populations. Whether glymphatic dysfunction contributes to development of conditions such as Alzheimer's disease remains to be directly tested. The present investigational device may permit the continuous and time-resolved assessment of key determinants of glymphatic function in naturalistic settings necessary to define whether glymphatic impairment contributes to risk and progression of Alzheimer's disease and its underlying pathological processes. The ability to assess glymphatic function over short timescales may enable target-engagement studies to identify and test pharmacological, device-based and lifestyle/behavioural interventions for modulating glymphatic function in humans. Assessment of these processes may also permit the identification of clinical populations with impaired glymphatic function who are at risk for the development of Alzheimer's disease, and who would thus be ideal candidates for therapeutic approaches targeting glymphatic clearance. Similar avenues now remain open outside the realm of neurodegenerative conditions as glymphatic dysfunction is implicated in an ever-increasing list of sleep-related neurological and psychiatric conditions.

Methods

Investigational device

System architecture. The Applied Cognition device is a wearable multisensor acquisition system that uses an STM32WB5MMG microcontroller (ST Microelectronics NV). It consists of a primary module housing the main electronics board and a 430 mAh Li-ion battery, two earpieces each housing one electrode, one accelerometer and one photoplethysmogram sensor, and two separate mastoid electrodes. A device schematic and visualization of signal outputs is provided in Fig. 2a–f. Sensor data are stored in an on-board FLASH memory and are downloaded via a USB port for offline analysis. The relevant subsystems are further described below. Device and PSG signal processing used open-source libraries Python 3.8.5, NumPy 1.21.6, SciPy 1.9.3, Pandas 1.5.2, Matplotlib 3.6.2, Seaborn 0.12.1, emd 0.6.2, Heartpy 1.2.7, yasa 0.6.3 and Impedance 1.4.

Electrical impedance spectroscopy. EIS was used to measure electrical impedance using the AFE4500 analogue front-end (AFE) from Texas Instruments. Four electrodes, two in-ear and two mastoid, were used to deliver the excitation current across the head and sense the resulting voltage. The two mastoid current injection sources were initially co-located inside the ear next to the Ag/AgCl sensors but, because of salt bridging, were externalized to the mastoids. In a departure from traditional four-electrode measurements, where excitation and sense electrodes are fixed, the AFE4500 was programmed to implement a technique developed by Texas Instruments where multiple excitation and sense configurations are used to determine the contact impedance and body impedance accurately.

Measurements were successively performed at 18 frequencies ranging from 1 kHz to 256 kHz following a logarithmic series, all with excitation current below 50 µA root mean square (rms). Frequencies were in alternating order from high to low to minimize any impact on impedance drift during each scan. Sensed voltages were quadrature demodulated, filtered and digitized internally by the AFE4500 to provide in-phase and out-of-phase components. Measurement time for each frequency was adjusted to give consistent signal-to-noise ratio across the frequency range, resulting in a scan time of 106 s.

Electroencephalogram. EEG was measured with an ADS1299-4 AFE from Texas Instruments, between the two in-ear electrodes (differential measurement). A third electrode (left mastoid) was used to drive the common mode. While these electrodes were shared with the EIS, the two measurements were time multiplexed and a pair of analogue multiplexers (TMUX1136, Texas Instruments) effectively decoupled EEG and EIS subcircuits and respective measurements. For EEG, both in-ear electrodes were also buffered (OPA376, Texas Instruments) in the earpiece. These buffers were bypassed (analogue multiplexer TMUX1136, Texas Instruments) for EIS or electrode impedance measurement.

The ADS1299-4 was programmed to have a sampling rate of 250 samples per second (24-bit samples) and an input range of ±180 mV. The common mode drive was actively derived from the in-ear electrodes. Both mastoid electrodes were also connected to an input channel so that the low-frequency (31.25 Hz) impedance of each electrode could be measured using the internal current source of the ADS1299-4. Such impedance measurements were performed before starting a recording session, and then automatically between EEG periods and EIS. EEG measurement periods were 170 s long, and the sequence EEG–EIS–electrode impedance repeated until the end of the recording session. A sample EEG spectrogram and hypnogram, derived from the device EEG is shown in Fig. 2b.

Impedance plethysmogram. In addition to impedance spectroscopy, real-time bioimpedance was acquired simultaneously with the EEG using the MAX30001 AFE (Analog Devices). The four-electrode configuration shared electrodes with the EEG, with the two mastoid electrodes used for current injection and the two in-ear electrodes for voltage sensing. A 96 µA current at 82 kHz was used for excitation. Such high-frequency excitation is effectively filtered by the ADS1299-4 and does not corrupt the EEG signal. The MAX30001 built-in synchronous demodulator filtered, and an analog-to-digital converter recovered the in-phase component of the sensed voltage and digitized it at 64 samples per second (20-bit resolution). The resulting impedance measurements had a noise floor of 3 mΩ rms (100 Ω load), enabling the detection of blood pulsations. A sample trace from a study participant, derived from the device IPG is shown in Fig. 2d. Note that the impedance shifts measured in either the respiratory or cardiac frequency bands ranged between 50 and 150 mΩ. In contrast, impedance shifts detected by EIS were at least an order of magnitude greater.

Photoplethysmogram and acceleration. In-ear reflective photoplethysmogram was measured with two miniature, fully integrated optical sensors (MAXM86161, Analog Devices) located in each earpiece, facing the anterior wall of the ear canal. One side was programmed to use green light (530 nm), while the other alternatively used red (660 nm) and infrared (880 nm) lights. To achieve a tight synchronization with EEG samples, the sensors ran at 1,024 Hz for each colour, and the most recent samples available at the time of the EEG read were averaged, resulting in a 250 Hz output rate and a phase variation <1 ms. A sample trace of the left (red) and right PPG (green) from a study participant is provided in Fig. 2f.

In-ear acceleration (X,Y,Z) was measured using two miniature MEMS Inertial Measurement Units (IMUs) (LSM6DSOX, ST Microelectronics NV) located in each earpiece. Similar to the PPG, the sensors were run at 833 Hz (each axis) and averaged to ensure tight time synchronization between sensors. A noise floor of 1 mg rms enabled the resolution of cardiac/blood pulsations, in addition to posture and activity. From these accelerometer data, a ballistocardiogram was derived, as shown for a study participant in Fig. 2e.

Electrodes. In-ear electrodes were laser cut from silver sheets 100 µm thick and 99.9% pure. The electrodes were 4.5-mm-diameter plates with a 1-mm-wide stem. The electrodes were abraded and sonicated in distilled water, dip coated with Ag/AgCl ink provided by Creative Materials (SKU EXP 2653-138-1) and cured at 100 °C for 60 min. Following curing, they were sintered at 427 °C for 60 min under low-flow argon gas.

Once fabricated, all electrodes were characterized according to the ANSI/AAMI EC12 standard for alternating current impedance[65], direct current (DC) offset voltage, combined offset instability and internal noise, and bias current tolerance (Supplementary Table 7). Pairs of electrodes were also connected to the earpiece circuits with clip-on wires and tested on an agar phantom as described in the 'Device testing' section.

Electrical impedance spectroscopy validation. Measurement accuracy was first evaluated using a test fixture simulating the load and the four electrodes (Supplementary Fig. 2). The load was either purely resistive (R, 20–100 Ω), or slightly reactive (2R1C, 20–100 Ω in parallel with 470 Ω and 22 nF in series) to mimic the brain parenchyma. The electrodes were implemented as either (1) low impedance (270 Ω resistor in series with a 1 kΩ resistor and 180 nF capacitor in parallel) or (2) high impedance (620 Ω resistor in series with a 3.3 kΩ resistor and 82 nF capacitor in parallel) to simulate the frequency dependence of typical Ag/AgCl electrodes, but also to ensure a minimal impedance at high frequencies. Two 10 Ω resistors were added between the electrodes connected to the same side of the load to simulate the tissue impedance between these electrodes as well. Supplementary Table 8 describes the benchtop tests performed, and Supplementary Tables 9 and 10 contain the results.

Device testing. In addition to the EIS test fixture, stability and reproducibility of EIS measurements over 12 h were evaluated with an agar phantom. A slab (5–10 mm thick) of conductive agar was first cast using a solution of 2.5% (weight) agar (Living Jin USA), 0.64% (weight) NaCl (RND Center) and distilled water. Electrodes (mastoids and earpieces for the final testing) were then coated with conductive gel (Electro-Gel, Electro-Cap International) to reduce the contact resistance, and placed on the agar slab in a pattern geometrically similar to the electrode location on the head. A 12-h recording was performed, resulting in a total of 450 min of EEG recording, 159 EIS cycles and 160 electrode impedance checks. The results of a 12-h agar phantom EEG test are shown in Supplementary Fig. 3.

Signal processing – parenchymal resistance. A Python neuroprocessing pipeline developed by Applied Cognition performed the data analysis of the signals captured by the investigational device. The neuroprocessing pipeline runs in the Amazon Web Services cloud on a distributed architecture allowing for fast parallel execution of participant device readings.

An EIS scan by the investigational device measured impedances $Z(\omega)$ at 18 frequencies $f(\omega = 2\pi f)$ ranging from 1,000 Hz to 256,000 Hz and took 106 s. The frequencies were measured in the following permuted order for each scan (all in Hz): 2,276, 102,400, 1,600, 64,000, 4,551, 51,200, 12,800, 85,333, 3,200, 25,600, 1,000, 32,000, 6,400, 8,533, 128,000, 204,800, 256,000. During the EIS scan, all other device sensors were powered off except the left in-ear IMU that sampled at 1 Hz to detect head motion and position. The EIS scans were duty cycled throughout the recording period with 165 s neurophysiology scans that captured data from the other sensors: EEG, PPGs and IMUs. Four electrode impedance checks at 30 Hz and lasting 7 s were performed during the neurophysiology scan and immediately preceding the EIS scan.

The Cole–Cole model[66–68] is commonly used to analyse EIS data. The analysis is based on the four parameters contained in the Cole equation R_0, R_∞, α and τ.

$$Z(\omega) = R_\infty + \frac{R_0 - R_\infty}{1 + (j\omega\tau)^\alpha}$$

As the excitation frequency ω ($\omega = 2\pi f$) increases to large values, the capacitive cell membranes are invisible to the excitation frequency, and the impedance $Z(\omega)$ approaches R_∞. The four excitation and response electrodes are positioned transcranially and at large ω, measure total intracranial brain volume. As the excitation frequency ω decreases approaching DC values, the capacitive cell membranes prevent any transmembrane conduction and the impedance $Z(\omega)$ approaches R_0, the measure of electrical resistance through extracellular fluid.

The value of τ in the Cole–Cole model is the inverse of tissue characteristic frequency $2\pi f_c$. The Cole–Cole α describes the divergence of a measured dielectric dispersion from the ideal dispersion exhibited by a Debye type of dielectric relaxation and is widely assumed to be related to a distribution of the relaxation times in the system involved. The value of α ranges from 0.5 to 1 with a value of 1 reducing the Cole–Cole model to the Debye model.

For each EIS scan, the four parameters were estimated using a nonlinear least-squares fit (Python SciPy's least_squares) with the trust region reflective algorithm that is a robust method suitable for large sparse problems with bounds. The α parameter was found to be close to 1 in the estimations and thereafter set to 1, reducing the Cole–Cole model to the Debye model. The remaining three parameters were estimated with bounds of 0–90 Ω for R_0, 0–70 Ω for R_∞ and bounds for $\tau = \frac{1}{2\pi f_c}$ determined by requiring the characteristic frequency f_c to lie between 16 kHz and 160 kHz. The parameter bounds were confirmed to encompass neurophysiological values in all participants by plotting all EIS scan resistance (real values of impedances $Z(\omega)$) and reactance (imaginary values of impedance $Z(\omega)$). Furthermore, no parameter solutions lay on a boundary for each scan across the range of dynamic impedance spectroscopy measurements for all participants.

Before fitting the Debye model to the EIS scan data to compensate for stray capacitance, time delay effects from signal transmission and electrical components, the impedances Z from each scan were rotated by multiplying by the factor $e^{-j\omega T}$, with the value T chosen so that the reactance at the highest frequency of the scan was zero[67]. This rotation was independently validated using EIS scans recorded on the benchtop tests using known impedance loads (Supplementary Table 10). The root mean squared error (RMSE) of the Debye model fits to the benchtop tests (Supplementary Table 8) are reported in Supplementary Table 11.

Each EIS scan measures R_P at a point in time, and to evaluate glymphatic function, the Debye model fits need to detect small changes in R_P. With the device time-multiplexing settings, the device completes ~84 scans over a 7-h night of sleep. The statistical models require significance testing of the mean change in R_P between sleep and wake, and testing significance of predictors of R_P in linear mixed models. These tests depend on the standard deviation of the Debye model dispersion and the number of EIS scans (Supplementary Table 12). Details of these analyses are found in Supplementary Information 4.

During EIS, tissue behaves as a linear, time-invariant and causal system allowing the use of Kramers–Kronig relations to identify electrical impedance measures that are corrupted by artefacts from motion, electrode impedances and other sources[37,38]. The Kramers–Kronig transform allows the real part of the electrical impedance measure to be derived from the imaginary part and vice versa[37]. These relations were used as validity tests for measured spectra. When the real and imaginary impedance measures did not satisfy the Kramers–Kronig relation, the measure was discarded. The Python PyEIS1.0.10 repository was used for Kramers–Kronig impedance validation. The validation uses the method of Schönleber[38] to avoid ambiguities in the linear Kramers–Kronig validity tests due to under- and overfitting.

In addition to the Kramers–Kronig validity tests, EIS measures were discarded if for any of the four electrode impedances, the difference across successive time measures exceeded 1 kΩ or if the EIS scan was collected during a wake interval on a participant randomized to sleep. The first condition ensured that the electrode impedances were maintained within a narrow range during the EIS scans and the second condition ensured that the EIS scans were representative of sleep physiology for participants randomized to sleep.

Signal processing – electroencephalography. The raw EEG tracings from the device and the commercial PSG (Philips Respironics Alice 6 LDx Diagnostic Sleep System) were time synchronized by time aligning a 100-ms square pulse generated by the device every 10 s and stored both in the device flash memory and in the PSG recording through an unused auxiliary analogue input channel. Each raw tracing was notch filtered at 60 Hz using a second-order infinite impulse response notch digital filter (Python SciPy 'iirnotch'). The digital filter was applied to the signal forward and backward with a combined filter phase of 0 (Python SciPy 'filtfilt'). The signal was then bandpass filtered between 0.3 Hz and 50 Hz using a finite impulse response filter with a Hann window (Python SciPy 'firwin). The length of the low-pass filter was 501 and the length of the high-pass filter was 2,401.

During the observation periods, participants were not allowed to touch devices that were plugged to power outlets. Other non-physiologic sources included excessive head motion that led to signal artefacts from the electrode–skin interface. Physiologic sources of signal artefact included electrooculogram, electrocardiogram and electromyogram. The signals were partitioned into time-aligned 30-s epochs. Epochs containing one or more peak-to-peak signal amplitude exceeding 350 μV or maximum power in the Welch power spectrum exceeding 1,000 $\mu V^2 Hz^{-1}$ were removed. In addition, the device in-ear (left and right) IMU signals were used to filter excessive motion by filtering epochs with peak-to-peak values on an x, y or z axis on either ear that exceeded 100 milli-g during sleep and 200 milli-g during wake.

The power spectral density of each 30-s epoch was computed using Welch's method[69] (Python Scipy 'welch') using 10-s segments and 50% overlap across successive segments. Relative powerbands were computed for delta power (1–4 Hz), theta power (4–8 Hz), alpha power (8–12 Hz), sigma power (12–15 Hz), beta power (15–30 Hz) and low gamma power (30–50 Hz), each normalized to the total power in the power spectral density. Simpson integration of the power spectral density was used for computing the total power and respective band powers.

Hypnogram staging of each 30-s epoch used automated scoring (Python yasa 0.6.3 'SleepStaging') trained and validated on 3,000 nights of data from the National Sleep Research Resource[70]. The automated scoring uses a single EEG derivative and a single electrooculogram (EOG) channel. For device hypnogram staging, the single in-ear transcranial derivative was used, and for the commercial PSG, hypnogram staging using C3-A2 and C4-A1 derivatives was recorded separately. The PSG left EOG channel was used for commercial PSG hypnogram staging. An additional T3–T4 transcranial PSG derivative was used for hypnogram staging as another comparison to the device's transcranial in-ear derivative. The internal agreement of commercial PSG and agreement between investigational device-based EEG and PSG are presented in Supplementary Table 6.

Signal processing – heart rate. The photoplethysmography left and right raw signals were bandpass filtered between 0.5 Hz and 10 Hz using a finite impulse response filter with a Hann window (Python SciPy 'firwin'). Empirical mode decomposition was used to identify peaks in the raw signals (Python emd 0.6.2) using a box-car rolling window of 100 observations[71]. Heart rate variability metrics were computed after removing outliers, ectopic beats and interpolating missing values (Python Aura-healthcare 'hrvanalysis'). Both time-domain features (standard deviation of the interbeat interval of normal sinus beats, 'sdnn') and frequency-domain features using the Lomb–Scargle periodogram (low-frequency signal power 'lf' between 0.04 and 0.15 Hz considered a mixture of sympathetic and parasympathetic activity, high-frequency signal power 'hf' between 0.15 and 0.4 Hz representing beat-to-beat changes from parasympathetic vagal activity, and the low-frequency to high-frequency ratio (lf:hf ratio)) were computed[72].

The device IMUs were located inside the left and right ear canal and provided left and right Cartesian coordinates of acceleration measured in milli-g, where 1,000 milli-g is the acceleration caused by earth's gravitational force. Each in-ear component from the device is uniquely and reproducibly oriented on account of the ellipsoidal shape of the human ear canal and the matching shape of the in-ear component. From this orientation, head position and motion (acceleration) were resolved from each set of IMU samples that included gross positions such as supine, reclined, upright, left and right.

Clinical study design. The investigational device was evaluated in two studies: a Benchmarking Study conducted in The Villages community in Florida in partnership with the UF Health PHRC and a Replication Study conducted at the University of Washington in Seattle. These studies were reviewed and approved by the University of Florida Institutional Review Board (IRB No. 202201364) and Western Institutional Review Board (IRB No. 20225818), respectively. Written informed consent was obtained from all study participants during a screening visit, before any study activities.

Participant recruitment. Following distribution of study flyers in public-facing locations in senior recreation and/or local medical centres, the Benchmarking Study enrolled 34 healthy participants 56–66 years of age, and the Replication Study enrolled 14 healthy participants 49–63 years of age. Participants were cognitively intact and had no history of clinical depression, confirmed during screening using the MoCA assessment and GDS scale. Other exclusion criteria included a history of diabetes, hypertension, coronary artery disease, pulmonary disease, neurological disease, or anxiety. Participants planning travel to alternate time zones within 2 weeks of study participation were also excluded. The CONSORT diagram for the Benchmarking

Study and Replication Study is provided in Fig. 3 (bottom), and participant exclusions are detailed in the Results section. Demographic data including age, sex, APOE4 allele status, MoCA and GDS for the Benchmarking Study, Replication Study and combined studies are provided in Supplementary Table 1.

Study protocol. As shown in the study schematic (Fig. 3, top), this was a cross-over study in which participants took part in two overnight study visits, one undergoing normal sleep and the other undergoing overnight sleep deprivation, at a 2–4-week interval. Each overnight study visit consisted of three study periods beginning at 19:00, 07:00 and 13:30 separated by two intervals: an overnight interval (23:00–06:30) and a morning interval (08:00–11:30).

Benchmarking study. Beginning with arrival to the study suite at 19:00, participants underwent a blood draw for APOE genotyping and assessment of amyloid β and tau biomarkers ($A\beta_{1-40}$, $A\beta_{1-42}$, phospho-tau181, phosho-tau217, non-phospho-tau181, non-phospho-tau217; C_2N Diagnostics[73–75]) and 60 min of non-contrast MRI scanning (sequences detailed below). On completion, participants were instrumented for commercial polysomnography (PSG, Philips Respironics Alice 6 LDx Diagnostic Sleep System) that included a 10–20 EEG montage with EOG and submental electromyogram (EMG). Electrode impedances were required to be below 5 kΩ. Participants were last instrumented with the investigational device, and device electrode impedances required to be below 5 kΩ.

The overnight interval lasted from 23:00 to 06:30 the following morning. To support study planning, participants were randomized to undergo either normal sleep or sleep deprivation for their initial overnight visit following completion of their informed consent, but this information was not shared with the participants. To reduce the likelihood of preparation bias on the part of participants (that is, altering sleep schedules or taking naps in anticipation of sleep deprivation visits), participants were not informed of their initial visit assignment until 4 pm the day of their arrival. Both PSG and investigational device recordings took place continuously throughout the overnight interval. Throughout the overnight period, sleep-assigned participants were allowed to sleep normally without interruption. Participants assigned to sleep deprivation were monitored by study staff to ensure adherence to the sleep deprivation protocol.

Between 07:00–07:45 the next morning, all participants were administered a cognitive battery that included the 5-min psychomotor vigilance test for sustained attention[76,77], symbol-digit modality test of processing speed, trail making test part A and part B for assessing executive function[78], and digit span forward test of working memory[79]. Following the cognitive battery, participants underwent a blood draw for amyloid β and tau biomarkers and a second non-contrast MRI scanning session (denoted T_0 in Results section). Immediately following the second non-contrast MRI scan, participants underwent intravenous GBCA injection (Gadavist, 0.1 mmol kg^{-1}), followed by T1- and T2-weighted contrast-enhanced MRI scans 7–10 min after GBCA injection (denoted T_{10} in Results section).

Participants were escorted back to the study suite where they were re-instrumented with the commercial PSG and the investigational device. The morning interval ran from 08:00 to 11:30. Participants assigned to the sleep condition in the overnight interval were required to remain awake and were monitored by study staff to ensure adherence; those assigned to the sleep deprivation condition in the overnight were allowed to sleep. During this interval, both the PSG and investigational device recorded data. The third assessment period commenced at the end of the morning interval. Participants underwent a final blood draw for amyloid β and tau biomarker assessment and then had a third MRI scanning session, including non-contrast sequences and T1- and T2-weighted contrast-enhanced sequences at ~4 h post GBCA injection (denoted T_{240} in Results section).

Replication study. The Replication protocol was an abridged version of the Benchmarking protocol. The inclusion/exclusion criteria were identical to the Benchmarking study except for the lower age cut-off. Participants were similarly randomized to a night of sleep or a night of sleep deprivation on their first visit, with a crossover to the alternative sleep/sleep deprivation assignment on their second visit. The protocol for the Replication Study was identical to that of the Benchmarking Study excepting that (1) participants did not undergo commercial PSG, sleep was assessed by investigational device EEG; (2) participant sleep deprivation adherence in the overnight interval was assessed retrospectively using the sleep EEG; (3) the cognitive battery did not include the digits forward working memory test; and (4) participants underwent only non-contrast and not contrast-enhanced MRI.

Cognitive assessments. The 5-min Psychomotor Vigilance Test from Texas A&M University System Computer Science and Engineering[80] and digits forward recall from Cambridge Cognition[79] were administered on an iPad. The paper-based Symbol Digit Modalities Test from Western Psychological Services[81], and Trail Making Test A and B[82], were administered by a clinical coordinator trained in administering these tests. The cognitive battery was administered in a quiet room with minimal distractions on the morning following sleep/wake and before the neuroimaging and phlebotomy. The administration of each test was preceded by the corresponding practice test. We have included a description of these tests within the overall protocol for completeness. The results of these cognitive tests and their relationship to investigational device outputs, sleep parameters, fluid biomarkers and MRI measures of glymphatic function will be reported elsewhere.

Plasma biomarkers. The APOE genotyping, amyloid β and tau plasma biomarkers were analysed using mass spectrometry by C_2N Diagnostics[83]. The sample collection procedure was provided by C_2N Diagnostics. Venipuncture and blood draw from the antecubital fossa were performed using a 22-gauge butterfly needle to minimize red blood cell haemolysis. A total of 10 ml of blood was drawn into a K_2 EDTA Vacutainer. The blood was centrifuged for 15 min using a swinging bucket rotor at 500–700 × g with the brake on. Immediately after centrifugation, four 1.0 ml plasma samples were aliquoted into 4 Sarstedt 2.0 ml micro tubes without disrupting the plasma per cell interface when transferring plasma. A calibrated air-displacement hand-held pipette with a polypropylene pipette tip was used. After aliquoting plasma into the Sarstedt micro tubes, the tubes were immediately capped and frozen at −40 °C. When the tubes were ready to be shipped to C_2N Diagnostics, they were packed into a plastic zip-lock bag with plenty of dry ice, placed in an absorbent towel and cryobox, and express couriered to C_2N Diagnostics priority overnight. In the present report, we utilized APOE4 allele status as a covariate in our analysis, and we have included a description of plasma biomarker assessment within the overall protocol for completeness. However, the fluid biomarker levels and their relationship to investigational device outputs, sleep parameters, cognitive tests and MRI measures will be reported elsewhere.

Magnetic resonance imaging approach. MRI scanning at The Villages site was conducted on a 3 T Siemens Vida system at Lake Medical Imaging, while scanning at the University of Washington site was conducted on a 3 T Philips Ingenia Elition X at the Diagnostic Imaging Sciences Center. In the present report, to define the relationship between brain R_P and glymphatic function, we utilized CE-MRI from Benchmarking Study participants following the overnight sleep condition. We have included a description of the other MRI-based approaches within the overall protocol for completeness. However, the relationship between these different MRI measures of glymphatic function, investigational device outputs, sleep parameters, cognitive tests and fluid biomarker levels will be reported elsewhere.

Contrast-enhanced MRI. Contrast-enhanced MRI involves intravenous administration of a gadolinium chelate that shortens T1, T2 and T2* relaxation parameters of the tissue it traverses through. Specifically, in this study, shortening of the T1 relaxation parameter enhances MRI signal that is proportional to the amount of gadolinium and its characteristic relaxivity. Gadolinium passes quickly through the cerebral and peripheral vasculature within the first 5–30 min. A fraction of the contrast enters the CSF and ISF[14,15] over many hours and finally, almost 99% of the contrast exits the body by renal clearance. The passage of intravenous GBCA from the vasculature to the CSF and ISF was measured in terms of a delayed signal enhancement at ~4 h after administration. Two previous studies have shown that delayed enhancement following contrast injection between 3 and 6 h is indicative of solute (in this case, GBCA) transport via the CSF–ISF glymphatic exchange[14,15]. At The Villages, we performed 3D T1-weighted magnetization-prepared rapid acquisition with gradient echo (MPRAGE) with TR/TI/TE = 2,300/900/2 ms, resolution = 1 × 1 × 1 mm^3, field of view = 256 × 256 × 208 mm^3 and total acquisition time = 5:12 min before contrast injection. The post-contrast MRI image (T_{10}) was acquired ~7–10 min after contrast injection, and its acquisition was identical to the pre-contrast image. A second post-contrast scan was acquired ~4 h (T_{240}) later using identical imaging parameters. Contrast-enhanced MRI signal processing used Python 3.8.5 with openly available packages FSL 6.0.5.1 and dcm2niix 1.0.20190902, and it included Matlab r2022b and Matlab libraries IVIM_lib and NIfTI_tools.

Structural MRI. Structural T1 MRI was used for classifying the brain tissue into lobar grey matter, lobar white matter and CSF, as well as for segmenting regions of interest including the hippocampus, sagittal sinus, internal carotid arteries, lateral ventricle and subarachnoid space. The T1 images were also used for registration purposes for all other imaging modalities. The T1 images were used for determining PVS morphometry[84,85]. Scanning parameters for the Benchmarking Study were identical to the contrast-enhanced MRI. Scanning parameters for the Replication Study were TR/TI/TE = 12/1,000/4.5 ms, resolution = 0.8 × 0.8 × 0.8 mm^3, field of view = 256 × 240 × 166 mm^3 and total acquisition time = 5:24 min. Since inclusion of T2 MRI significantly improves PVS detection, a T2 MRI with TR/TE = 3,200/561 ms, resolution = 0.8 × 0.8 × 0.8 mm^3, field of view = 256 × 240 × 166 mm^3 and total acquisition time = 4:32 min were also added.

Intravoxel incoherent motion MRI. Intravoxel incoherent motion (IVIM) MRI is a multishell diffusion imaging approach to measure water movement at different scales of distance and time. Glymphatic transport includes movement of CSF in the subarachnoid space and the interstitium at a slow speed (~1 mm s^{-1}) over large distances (~100–200 µm)[1,26,43]. This perivascular movement of CSF through the subarachnoid compartment is upstream of its exchange with the ISF along the penetrating intraparenchymal vasculature, hence it could serve as an important correlate of glymphatic function[86]. The imaging parameters for the Benchmarking Study were: TR/TE = 5,500/124 ms, resolution = 1 × 1 × 5 mm^3, field of view = 250 × 250 × 150 mm^3, parallel imaging factor = 2, multiband factor = 3, fat suppression with spectral presaturation with inversion recovery (SPIR), b values = 0, 50, 100, 150, 200, 250, 300, 350, 400, 500, 700, 800 and 1,000 s mm^{-2}, and total acquisition time = 7:01 min. The b = 0 s mm^{-2} was acquired with reverse phase encoding to correct for field distortions. The imaging parameters for the Replication Study were TR/TE = 2,978/90 ms, resolution = 1 × 1 × 5 mm^3, parallel imaging factor = 2.2, field of view = 230 × 196 × 115 mm^3, fat suppression with SPIR, b values = 0, 10, 40, 80, 100, 150, 200, 300, 500, 700, 800, 900 and 1,000 s mm^{-2}, and total acquisition time = 8:08 min. A Split echo (SPLICE) acquisition was used to eliminate the need for distortion correction.

Multi-echo, multidelay arterial spin labelling (ASL) MRI. Multi-echo, multidelay ASL measures perfusion and time for exchange of water across the endothelium. This time metric is dependent on perfusion, endothelial permeability and the glial vascular unit including the AQP4 water channels that are critical to the perivascular CSF–ISF exchange[86,87]. This protocol was implemented only for the Replication Study as a Hadamard-encoded ASL acquisition, TR/TE = 5,000 ms, resolution = 3.75 × 3.75 × 5 mm^3, field of view = 230 × 196 × 115 mm^3, post-labelling delay = 650, 950, 1,210, 1,510, 2,083 and 2,383 ms with background suppression, label duration = 3,400 ms and TE = 0, 40, 80 and 120 ms. Total acquisition time = 12:40 min. A conventional ASL protocol was implemented in the Benchmarking Study due to inavailability of the multi-echo component. The parameters were: TR/TE = 4,420/22 ms, resolution = 1.7 × 1.7 × 4 mm^3, field of view = 220 × 220 × 96 mm^3, post-labelling delay = 500, 900, 1,000, 1,100, 1,200, 1,400, 1,600 and 1,800, label duration = 1,800 ms. Total acquisition time = 2:37 min. The sequence was acquired twice. Reference M0 images were acquired in both studies with identical parameters but without background suppression or labelling.

Fast functional MRI. A subsecond functional MRI sequence was implemented to separate and regress physiological noise (cardiac and respiratory signals) as well as to capture slow CSF oscillations in the ventricles[88]. The protocol for the Benchmarking Study was TR/TE = 400–500 per 30 ms, resolution = 3.6 × 3.6 × 3.6 mm^3, flip angle = 70°, multiband factor = 4, field of view = 230 × 2,430 × 101 mm^3, fat suppression, no. of volumes = 365 using SPIR, total acquisition time = 2:37 min. Heart rate and respiration were monitored using the BIOPAC MR160 and synchronized with MRI acquisition. The Replication Study used a gradient-echo, echo planar imaging sequence with TR/TE = 400–500 per 30 ms, resolution = 3 × 3 × 4 mm^3, flip angle = 42°, multiband factor = 6, field of view = 240 × 240 × 123 mm^3, slice gap = 0.4 mm, fat suppression using SPIR, no. of volumes = 450, total acquisition time = 3:00 min. Two single-volume, spin echo acquisitions were also acquired with opposite phase encoding to allow for distortion correction. Heart rate and respiration were monitored using the sensors built into the Philips scanner and synchronized with MRI acquisition. Glymphatic CSF–ISF exchange is at least partly driven by vasomotion, which may be reflected by periodic motion in the CSF spaces. This CSF motion correlates well with sleep stages, with power of the slow CSF oscillation increasing from wakefulness to the N1 and finally to the N2 stage[88].

Phase-contrast MRI. The phase-contrast MRI was used to quantify CSF efflux from the Aqueduct of Sylvius. The peristaltic motion of CSF at the Aqueduct was measured by gating the MRI signal to the participants and calculating the CSF motion into and out of the brain over a cardiac signal. Variations in CSF efflux velocity appeared to follow the cardiac and respiratory signals and might impact glymphatic CSF–ISF exchange. The Benchmarking Study protocol for this MRI was as follows: a single-slice acquisition perpendicular to the Aqueduct of Sylvius, TR/TE = 21/6.6 ms, resolution = 30.6 × 0.6 × 6 mm^3, flip angle = 10°, 40 phases per cardiac cycle, velocity encoding for 12 cm s^{-1}, total acquisition time: 2:00 min. The Replication Study protocol included the following: a single-slice acquisition perpendicular to the Aqueduct of Sylvius, TR/TE = 12/7.9 ms, resolution = 30.6 × 0.6 × 4 mm^3, flip angle = 10°, 15 phases per cardiac cycle, velocity encoding for 12 cm s^{-1}, total acquisition time: 2:02 min

Statistical approach. The Benchmarking study was designed to have 80% power at a significance level of 5% to detect a low to moderate correlation r (r = 0.5) between the device measurements and CE-MRI measurement of glymphatic function. The Replication study was designed to have 80% power at a significance level of 20% to detect a low to moderate correlation r (r = 0.5) between the device measurements and non-contrast MRI measurement of glymphatic function and to detect overnight sleep/wake differences in brain parenchymal resistance.

The parenchymal resistances R_P computed from each EIS scan from the device were normalized to the sleep/wake onset values to allow comparison across visits and participants. To reduce measurement variability of the sleep/wake onset value, the value was inferred from a linear regression to the initial R_P values. The overnight change in R_P per participant visit was taken as the average of the normalized values for that visit. For example, a value of 1 indicated that there was no overnight change from the onset value and a value of 0.8 indicated a 20% overnight reduction from onset. A Student's *t*-test group comparison between sleep/wake visits, group means and standard deviations were calculated.

Contrast-enhanced MRI of sleep-related glymphatic function was analysed using a random intercept linear mixed effect model (R, lme in the lmne package). Glymphatic function was defined by measuring brain parenchymal contrast enhancement, the % change in T1-weighted signal intensity between 10 and 240 min post GBCA injection (100% × $(T_{240}-T_{10})/T_0$) at each of 8 ROIs: frontal cortical grey and white matter, parietal cortical grey and white matter, temporal cortical grey and white matter, and occipital grey and white matter. Only sleep visits were analysed leading to one level of grouping, the 8 ROIs, for the participant sleep visit. All models included regressors in the mixed model for the $T_{10}-T_{240}$ change in blood signal within the internal carotid artery, and the $T_{10}-T_{240}$ change in CSF signal within the cerebral lateral ventricles to compensate for the influence of vascular and CSF contrast on parenchymal enhancement. Potentially confounding biological variables age, gender and APOE ε4 status were also included in all models.

To evaluate different sleep-related contributions to glymphatic function, overnight changes from sleep onset for each of the 4 recorded EEG relative band powers (delta, theta, alpha, beta) and for HR were computed. The recorded values were normalized to their respective values at sleep onset and a single statistic, the average of the overnight normalized values, computed per participant visit. The 4 hypnogram sleep stages (N1, N2, N3, REM) and WASO were each summed into single total sleep stage durations and total WASO duration per participant visit. The device R_P normalization and averaging has been previously described. Models were run separately for each of the 4 EEG relative band powers (delta, theta, alpha, beta), for each of the 4 hypnogram sleep stages (N1, N2, N3, REM), for WASO, for HR and for device R_P. Two full models were then fit to the data, with the EEG band power and the hypnogram sleep stages separated into distinct models because of collinearity across those predictors. The variance inflation factor (R 'vif' function in the 'car' package) was used to test for predictor collinearity using a threshold of 5. The EEG powerbands included were limited to delta, theta and beta because of collinearity among the 4 relative band powers. HR and the device R_P were included in both full models. Each full model was reduced to a selected model using backward elimination of predictors with a threshold Wald's *P* value of 0.05.

Model selection stability, or robustness of the selected model to perturbations in the dataset, was tested using resampling-based multimodel inference[36]. The dataset was bootstrap resampled with replacement to generate 500 bootstrapped datasets. For each of these datasets, the two full models were estimated and reduced to a selected model using backward elimination. The bootstrap inclusion frequency (the percent of bootstrap datasets included the predictor), the RMSD ratio (the RMSD of the predictor bootstrap estimate divided by the standard error of that coefficient in the full model and expressing the variance inflation or deflation caused by variable selection), the relative conditional bias (quantifying the variable-selection-induced bias to expect if a predictor is selected) and the bootstrap median of each predictor coefficient were reported.

The analyses of device R_P values with EEG band powers, heart rate and hypnogram staging were performed on the overnight sleep recordings. Analyses were grouped into REM sleep and NREM sleep (N1, N2 and N3). The device resistances were computed repeatedly throughout the night from each EIS scan. During sleep recordings, these data were non-stationary. After normalization to sleep onset as previously described, first-order differences ΔR_P and ΔX for one (X) of the EEG band powers or HR were incorporated into individual random intercept linear mixed models to evaluate their relationship. Threshold regression models were used in the linear mixed model. A custom estimation procedure described in Supplementary Information was used to jointly estimate the threshold regression for the full positive and negative range of the predictors. The hinge threshold model was analytically reduced to estimation by linear regression, which allowed it to be used in a random intercepts linear mixed effects regression model. The autocorrelation function and augmented Dickey Fuller tests were used to confirm stationarity of the differenced variables ΔR_P and ΔX, and also of the fitted model residuals (R, acf and adf functions).

In addition to the analyses of ΔR_P and ΔX for one (X) of the EEG powerbands or HR during REM sleep and NREM sleep, these were analysed at hypnogram transitions NREM to REM, REM to NREM, sleep to wake and wake to sleep. The analysis was similar, using threshold regression models in a random intercept mixed linear model.

Univariate outliers were trimmed at the 0.5 and 99.5 percentile. For multivariate analysis, the Mahalonobis distance was computed and outliers trimmed at the 0.5 and 99.5 percentile of the Mahalonobis distance. All regressions were adjusted for potential confounding effects of age, sex and APOE genotype. All tests were considered significant at the 5% level if the 95% CI did not contain the null hypothesis. All statistical analyses were performed in R v.4.2.1 (2022-06-23).

We report the pooled findings of the Benchmarking and Replication studies for both the investigational device transcranial resistance measurements and EEG parameters.

Reporting summary

Further information on research design is available in the Nature Portfolio Reporting Summary linked to this article.

Data availability

The human participant data supporting this study are available on Zenodo at https://doi.org/10.5281/zenodo.15059617 (ref. 89). Access requires Institutional Review Board (IRB) approval and a completed Data User Agreement (DUA). A blank DUA can be found at https://tinyurl.com/appliedcognition-dua. To obtain access, please submit IRB approval and completed DUA to the corresponding author or research@appliedcognition.com.

Code availability

Code used for the analysis and to produce the figures are available on Zenodo at https://doi.org/10.5281/zenodo.15059532 (ref. 90).

References

1. Iliff, J. J. et al. A paravascular pathway facilitates CSF flow through the brain parenchyma and the clearance of interstitial solutes, including amyloid β. *Sci. Transl. Med.* **4**, 147ra111 (2012).
2. Xie, L. et al. Sleep drives metabolite clearance from the adult brain. *Science* **342**, 373–377 (2013).
3. Iliff, J. J. et al. Impairment of glymphatic pathway function promotes tau pathology after traumatic brain injury. *J. Neurosci.* **34**, 16180–16193 (2014).
4. Harrison, I. F. et al. Impaired glymphatic function and clearance of tau in an Alzheimer's disease model. *Brain* **143**, 2576–2593 (2020).
5. Ishida, K. et al. Glymphatic system clears extracellular tau and protects from tau aggregation and neurodegeneration. *J. Exp. Med.* **219**, e20211275 (2022).
6. Cui, H. et al. Decreased AQP4 expression aggravates α-synuclein pathology in Parkinson's disease mice, possibly via impaired glymphatic clearance. *J. Mol. Neurosci.* **71**, 2500–2513 (2021).

7. Zou, W. et al. Blocking meningeal lymphatic drainage aggravates Parkinson's disease-like pathology in mice overexpressing mutated α-synuclein. *Transl. Neurodegener.* **8**, 7 (2019).
8. Hablitz, L. M. & Nedergaard, M. The glymphatic system: a novel component of fundamental neurobiology. *J. Neurosci.* **41**, 7698–7711 (2021).
9. Klostranec, J. M. et al. Current concepts in intracranial interstitial fluid transport and the glymphatic system: Part II–imaging techniques and clinical applications. *Radiology* **301**, 516–532 (2021).
10. Hablitz, L. M. et al. Circadian control of brain glymphatic and lymphatic fluid flow. *Nat. Commun.* **11**, 4411 (2020).
11. Hablitz, L. M. et al. Increased glymphatic influx is correlated with high EEG delta power and low heart rate in mice under anesthesia. *Sci. Adv.* **5**, eaav5447 (2019).
12. Eide, P. K., Vinje, V., Pripp, A. H., Mardal, K. A. & Ringstad, G. Sleep deprivation impairs molecular clearance from the human brain. *Brain* **144**, 863–874 (2021).
13. Ringstad, G. et al. Brain-wide glymphatic enhancement and clearance in humans assessed with MRI. *JCI Insight* https://doi.org/10.1172/jci.insight.121537 (2018).
14. Deike-Hofmann, K. et al. Glymphatic pathway of gadolinium-based contrast agents through the brain: overlooked and misinterpreted. *Invest. Radio.* **54**, 229–237 (2019).
15. Richmond, S. B. et al. Quantification approaches for magnetic resonance imaging following intravenous gadolinium injection: a window into brain-wide glymphatic function. *Eur. J. Neurosci.* **57**, 1689–1704 (2023).
16. Bera, T. K. Bioelectrical impedance methods for noninvasive health monitoring: a review. *J. Med. Eng.* **2014**, 381251 (2014).
17. Abasi, S., Aggas, J. R., Garayar-Leyva, G. G., Walther, B. K. & Guiseppi-Elie, A. Bioelectrical impedance spectroscopy for monitoring mammalian cells and tissues under different frequency domains: a review. *ACS Meas. Sci. Au* **2**, 495–516 (2022).
18. Stupin, D. D. et al. Bioimpedance spectroscopy: basics and applications. *ACS Biomater. Sci. Eng.* **7**, 1962–1986 (2021).
19. Gabriel, S., Lau, R. W. & Gabriel, C. The dielectric properties of biological tissues: II. Measurements in the frequency range 10 Hz to 20 GHz. *Phys. Med. Biol.* **41**, 2251–2269 (1996).
20. Gabriel, C. Dielectric properties of biological tissue: variation with age. *Bioelectromagnetics* https://doi.org/10.1002/bem.20147 (2005).
21. Jessen, N. A., Munk, A. S., Lundgaard, I. & Nedergaard, M. The glymphatic system: a beginner's guide. *Neurochem. Res.* **40**, 2583–2599 (2015).
22. Nakamura, K. et al. Diurnal fluctuations in brain volume: statistical analyses of MRI from large populations. *Neuroimage* **118**, 126–132 (2015).
23. Elvsåshagen, T. et al. Cerebral blood flow changes after a day of wake, sleep, and sleep deprivation. *Neuroimage* **186**, 497–509 (2019).
24. van Veluw, S. J. et al. Vasomotion as a driving force for paravascular clearance in the awake mouse brain. *Neuron* **105**, 549–561.e5 (2020).
25. Iliff, J. J. et al. Cerebral arterial pulsation drives paravascular CSF-interstitial fluid exchange in the murine brain. *J. Neurosci.* **33**, 18190–18199 (2013).
26. Mestre, H. et al. Flow of cerebrospinal fluid is driven by arterial pulsations and is reduced in hypertension. *Nat. Commun.* **9**, 4878 (2018).
27. Jiang-Xie, L. F. et al. Neuronal dynamics direct cerebrospinal fluid perfusion and brain clearance. *Nature* **627**, 157–164 (2024).
28. Murdock, M. H. et al. Multisensory gamma stimulation promotes glymphatic clearance of amyloid. *Nature* **627**, 149–156 (2024).
29. Helakari, H. et al. Human NREM sleep promotes brain-wide vasomotor and respiratory pulsations. *J. Neurosci.* **42**, 2503–2515 (2022).
30. Kress, B. T. et al. Impairment of paravascular clearance pathways in the aging brain. *Ann. Neurol.* **76**, 845–861 (2014).
31. Dagum, P. et al. Non-invasive assessment of glymphatic flow and neurodegeneration from a wearable device. US Patent 11,478,184 B1 (2022).
32. Dagum, P. & Giovangrandi, L. B. Non-invasive topographic localization of glymphatic flow. US Patent 12,133,738 B2 (2024).
33. Nasreddine, Z. S. et al. The Montreal Cognitive Assessment, MoCA: a brief screening tool for mild cognitive impairment. *J. Am. Geriatr. Soc.* **53**, 695–699 (2005).
34. Brown, L. M. & Schinka, J. A. Development and initial validation of a 15-item informant version of the Geriatric Depression Scale. *Int. J. Geriatr. Psychiatry* **20**, 911–918 (2005).
35. *Gadavist (Gadobutrol) Injection, for Intravenous Use* (FDA, 2011); https://www.accessdata.fda.gov/drugsatfda_docs/label/2011/201277s000lbl.pdf
36. Heinze, G., Wallisch, C. & Dunkler, D. Variable selection - A review and recommendations for the practicing statistician. *Biom. J.* **60**, 431–449 (2018).
37. Boukamp, B. A. A linear Kronig–Kramers transform test for immittance data validation. *J. Electrochem. Soc.* **142**, 1885 (1995).
38. Schonleber, M., Klotz, D. & Ivers-Tiffee, E. A method for improving the robustness of linear Kramers–Kronig validity tests. *Electrochim. Acta* **131**, 20–27 (2014).
39. Song, J. et al. Electrical impedance changes at different phases of cerebral edema in rats with ischemic brain injury. *BioMed. Res. Int.* **2018**, 9765174 (2018).
40. Abboud, T., Mielke, D. & Rohde, V. Mini review: impedance measurement in neuroscience and its prospective application in the field of surgical neurooncology. *Front. Neurol.* **12**, 825012 (2021).
41. Witkowska-Wrobel, A., Aristovich, K., Crawford, A., Perkins, J. D. & Holder, D. Imaging of focal seizures with electrical impedance tomography and depth electrodes in real time. *Neuroimage* **234**, 117972 (2021).
42. Romsauerova, A. et al. Multi-frequency electrical impedance tomography (EIT) of the adult human head: initial findings in brain tumours, arteriovenous malformations and chronic stroke, development of an analysis method and calibration. *Physiol. Meas.* **27**, S147–S161 (2006).
43. Iliff, J. J. et al. Brain-wide pathway for waste clearance captured by contrast-enhanced MRI. *J. Clin. Invest.* **123**, 1299–1309 (2013).
44. Eide, P. K. & Ringstad, G. MRI with intrathecal MRI gadolinium contrast medium administration: a possible method to assess glymphatic function in human brain. *Acta Radio. Open* **4**, 2058460115609635 (2015).
45. Lee, S. et al. Contrast-enhanced MRI T1 mapping for quantitative evaluation of putative dynamic glymphatic activity in the human brain in sleep–wake states. *Radiology* **300**, 661–668 (2021).
46. Mestre, H. et al. Aquaporin-4-dependent glymphatic solute transport in the rodent brain. *Elife* https://doi.org/10.7554/eLife.40070 (2018).
47. Groothuis, D. R. et al. Efflux of drugs and solutes from brain: the interactive roles of diffusional transcapillary transport, bulk flow and capillary transporters. *J. Cereb. Blood Flow Metab.* **27**, 43–56 (2007).
48. Benveniste, H. et al. Anesthesia with dexmedetomidine and low-dose isoflurane increases solute transport via the glymphatic pathway in rat brain when compared with high-dose isoflurane. *Anesthesiology* **127**, 976–988 (2017).

49. Stanton, E. H. et al. Mapping of CSF transport using high spatiotemporal resolution dynamic contrast-enhanced MRI in mice: effect of anesthesia. *Magn. Reson. Med.* **85**, 3326–3342 (2021).
50. Ozturk, B. O. et al. Disparate volumetric fluid shifts across cerebral tissue compartments with two different anesthetics. *Fluids Barriers CNS* **18**, 1 (2021).
51. Gakuba, C. et al. General anesthesia inhibits the activity of the 'glymphatic system. *Theranostics* **8**, 710–722 (2018).
52. Miao, A. et al. Brain clearance is reduced during sleep and anesthesia. *Nat. Neurosci.* **27**, 1046–1050 (2024).
53. Piantino, J., Lim, M. M., Newgard, C. D. & Iliff, J. Linking traumatic brain injury, sleep disruption and post-traumatic headache: a potential role for glymphatic pathway dysfunction. *Curr. Pain Headache Rep.* **23**, 62 (2019).
54. Nedergaard, M. & Goldman, S. A. Glymphatic failure as a final common pathway to dementia. *Science* **370**, 50–56 (2020).
55. Goldman, N., Hablitz, L. M., Mori, Y. & Nedergaard, M. The glymphatic system and pain. *Med. Acupunct.* **32**, 373–376 (2020).
56. Braun, M. & Iliff, J. J. The impact of neurovascular, blood-brain barrier, and glymphatic dysfunction in neurodegenerative and metabolic diseases. *Int. Rev. Neurobiol.* **154**, 413–436 (2020).
57. Wang, M. et al. Focal solute trapping and global glymphatic pathway impairment in a murine model of multiple microinfarcts. *J. Neurosci.* **37**, 2870–2877 (2017).
58. Li, M. et al. Impaired glymphatic function and pulsation alterations in a mouse model of vascular cognitive impairment. *Front. Aging Neurosci.* **13**, 788519 (2021).
59. Xu, Z. et al. Deletion of aquaporin-4 in APP/PS1 mice exacerbates brain Aβ accumulation and memory deficits. *Mol. Neurodegener.* **10**, 58 (2015).
60. Simon, M. et al. Loss of perivascular aquaporin-4 localization impairs glymphatic exchange and promotes amyloid β plaque formation in mice. *Alzheimers Res. Ther.* **14**, 59 (2022).
61. Pedersen, T. J., Keil, S. A., Han, W., Wang, M. X. & Iliff, J. J. The effect of aquaporin-4 mis-localization on Aβ deposition in mice. *Neurobiol. Dis.* **181**, 106100 (2023).
62. Burfeind, K. G. et al. The effects of noncoding aquaporin-4 single-nucleotide polymorphisms on cognition and functional progression of Alzheimer's disease. *Alzheimers Dement.* **3**, 348–359 (2017).
63. Zeppenfeld, D. M. et al. Association of perivascular localization of aquaporin-4 with cognition and Alzheimer disease in aging brains. *JAMA Neurol.* **74**, 91–99 (2017).
64. Simon, M. J. et al. Transcriptional network analysis of human astrocytic endfoot genes reveals region-specific associations with dementia status and tau pathology. *Sci. Rep.* **8**, 12389 (2018).
65. *ANSI/AAMI EC12:2000 (R2020)* (ANSI, 2020).
66. Ayllon, D., Seoane, F. & Gil-Pita, R. Cole equation and parameter estimation from electrical bioimpedance spectroscopy measurements – a comparative study. *Annu. Int. Conf. IEEE Eng. Med. Biol. Soc.* **2009**, 3779–3782 (2009).
67. De Lorenzo, A., Andreoli, A., Matthie, J. & Withers, P. Predicting body cell mass with bioimpedance by using theoretical methods: a technological review. *J. Appl. Physiol.* **82**, 1542–1558 (1997).
68. Gabriel, S., Lau, R. W. & Gabriel, C. The dielectric properties of biological tissues: III. Parametric models for the dielectric spectrum of tissues. *Phys. Med. Biol.* **41**, 2271–2293 (1996).
69. Welch, P. The use of the fast Fourier transform for the estimation of power spectra: a method based on time averaging over short, modified periodograms. *IEEE Trans. Audio Electroacoust.* **15**, 70–73 (1967).
70. Vallat, R. & Walker, M. P. An open-source, high-performance tool for automated sleep staging. *Elife* https://doi.org/10.7554/eLife.70092 (2021).
71. Quinn, A. J., Lopes-Dos-Santos, V., Dupret, D., Nobre, A. C. & Woolrich, M. W. EMD: Empirical Mode Decomposition and Hilbert-Huang spectral analyses in Python. *J. Open Source Softw.* https://doi.org/10.21105/joss.02977 (2021).
72. Heart rate variability: standards of measurement, physiological interpretation and clinical use. Task Force of the European Society of Cardiology and the North American Society of Pacing and Electrophysiology. *Circulation* **93**, 1043–1065 (1996).
73. Janelidze, S. et al. Head-to-head comparison of 8 plasma amyloid-β 42/40 assays in Alzheimer disease. *JAMA Neurol.* **78**, 1375–1382 (2021).
74. Roberts, K. F. et al. Amyloid-β efflux from the central nervous system into the plasma. *Ann. Neurol.* **76**, 837–844 (2014).
75. Liu, H. et al. Acute sleep loss decreases CSF-to-blood clearance of Alzheimer's disease biomarkers. *Alzheimers Dement.* https://doi.org/10.1002/alz.12930 (2023).
76. Loh, S., Lamond, N., Dorrian, J., Roach, G. & Dawson, D. The validity of psychomotor vigilance tasks of less than 10-minute duration. *Behav. Res. Methods Instrum. Comput.* **36**, 339–346 (2004).
77. Arsintescu, L. et al. Validation of a touchscreen psychomotor vigilance task. *Accid. Anal. Prev.* **126**, 173–176 (2019).
78. Arbuthnott, K. & Frank, J. Trail making test, part B as a measure of executive control: validation using a set-switching paradigm. *J. Clin. Exp. Neuropsychol.* **22**, 518–528 (2000).
79. *Digit Span (DGS)* (Cambridge Cognition, 2022); https://cambridgecognition.com/digit-span-dgs/
80. *PVT Research Tool* (Apple, 2022); https://apps.apple.com/tr/app/pvt-research-tool/id1475726298
81. Smith, A. *Symbol Digit Modalities Test* (Western Psychological Association, 1992).
82. Reitan, R. *Trail Making Test: Manual for Administration and Scoring* (ScienceOpen, 1992).
83. *Developing and Commercializing Novel Diagnostics for Alzheimer's Disease and Related Forms of Neurodegeneration to Improve Treatment Decisions and Patients' Lives* (C_2N Diagnostics, 2023); https://c2n.com
84. Piantino, J. et al. Link between mild traumatic brain injury, poor sleep, and magnetic resonance imaging: visible perivascular spaces in veterans. *J. Neurotrauma* **38**, 2391–2399 (2021).
85. Boespflug, E. L. et al. MR imaging-based multimodal autoidentification of perivascular spaces (mMAPS): automated morphologic segmentation of enlarged perivascular spaces at clinical field strength. *Radiology* **286**, 632–642 (2018).
86. Levendovszky, S. R. et al. Preliminary investigations into human neurofluid transport using multiple novel non-contrast MRI methods. *J. Cereb. Blood Flow Metab.* https://doi.org/10.1177/0271678X241264407 (2024).
87. Ohene, Y. et al. Non-invasive MRI of brain clearance pathways using multiple echo time arterial spin labelling: an aquaporin-4 study. *Neuroimage* **188**, 515–523 (2019).
88. Fultz, N. E. et al. Coupled electrophysiological, hemodynamic, and cerebrospinal fluid oscillations in human sleep. *Science* **366**, 628–631 (2019).
89. Applied Cognition, Inc. A wireless device for continuous measurement of brain parenchymal resistance tracks glymphatic function in humans) (1.0.1) [Data set]. *Zenodo* https://doi.org/10.5281/zenodo.15059617 (2025).
90. Dagum, P., Singh T. & Corbellini, A. A wireless device for continuous measurement of brain parenchymal resistance tracks glymphatic function in humans. Code_202503.zip. *Zenodo* https://doi.org/10.5281/zenodo.15059532 (2025).

Acknowledgements

This work was funded by Applied Cognition.

Author contributions

P.D. and J.J.I. conceptualized the study. S.R.L., T.S. and C.V. collected and managed the data. P.D., T.S., Y.C. and R.M.K. performed formal analyses. P.D., L.G. and S.R.L. developed experimental methods. P.D. wrote the original draft. P.D., L.G., S.R.L., J.J.W., T.S., Y.C., R.M.K., M.S.J., M.M.L., C.V. and J.J.I. revised and edited the paper.

Competing interests

P.D., L.G., S.R.L., J.W., T.S., M.M.L. and J.J.I. declare the existence of financial and stock options. Y.C. and R.M.K. declare the existence of financial competing interests.

Additional information

Supplementary information The online version contains supplementary material available at https://doi.org/10.1038/s41551-025-01394-9.

Correspondence and requests for materials should be addressed to Paul Dagum.

Peer review information *Nature Biomedical Engineering* thanks Dean Pountney, Vesa Kiviniemi and Ysbrand Van der Werf for their contribution to the peer review of this work.

---

[1]Applied Cognition Inc., Redwood City, CA, USA. [2]Department of Radiology, University of Washington School of Medicine, Seattle, WA, USA. [3]VISN 20 NW Mental Illness Research, Education and Clinical Center, VA Puget Sound Healthcare System, Seattle, WA, USA. [4]Clinical Excellence Research Center, Stanford University School of Medicine, Stanford, CA, USA. [5]Department of Neurology, University of Florida Health, Gainesville, FL, USA. [6]UF Brain injury, Rehabilitation, and Neuroresilience Center, University of Florida, Gainesville, FL, USA. [7]VISN 20 Northwest Mental Illness Research, Education and Clinical Center (MIRECC), VA Portland Health Care System, Portland, OR, USA. [8]Neurology Service, Research Service, VA Portland Health Care System, Portland, OR, USA. [9]Department of Neurology, Oregon Alzheimer's Disease Research Center, Oregon Health and Science University, Portland, OR, USA. [10]University of Florida Health Precision Health Research Center, Clinical and Translational Science Institute, University of Florida, Gainesville, FL, USA. [11]Health Outcomes and Biomedical Informatics, College of Medicine, University of Florida, Gainesville, FL, USA. [12]Department of Psychiatry and Behavioral Science, University of Washington School of Medicine, Seattle, WA, USA. [13]Department of Neurology, University of Washington School of Medicine, Seattle, WA, USA. ✉e-mail: paul@appliedcognition.com

nature portfolio

Corresponding author(s): Paul Dagum, MD PhD

Last updated by author(s): 3/21/2025

Reporting Summary

Nature Portfolio wishes to improve the reproducibility of the work that we publish. This form provides structure for consistency and transparency in reporting. For further information on Nature Portfolio policies, see our Editorial Policies and the Editorial Policy Checklist.

Statistics

For all statistical analyses, confirm that the following items are present in the figure legend, table legend, main text, or Methods section.

n/a	Confirmed	
☐	☒	The exact sample size (*n*) for each experimental group/condition, given as a discrete number and unit of measurement
☐	☒	A statement on whether measurements were taken from distinct samples or whether the same sample was measured repeatedly
☐	☒	The statistical test(s) used AND whether they are one- or two-sided *Only common tests should be described solely by name; describe more complex techniques in the Methods section.*
☐	☒	A description of all covariates tested
☐	☒	A description of any assumptions or corrections, such as tests of normality and adjustment for multiple comparisons
☐	☒	A full description of the statistical parameters including central tendency (e.g. means) or other basic estimates (e.g. regression coefficient) AND variation (e.g. standard deviation) or associated estimates of uncertainty (e.g. confidence intervals)
☐	☒	For null hypothesis testing, the test statistic (e.g. *F*, *t*, *r*) with confidence intervals, effect sizes, degrees of freedom and *P* value noted *Give P values as exact values whenever suitable.*
☒	☐	For Bayesian analysis, information on the choice of priors and Markov chain Monte Carlo settings
☐	☒	For hierarchical and complex designs, identification of the appropriate level for tests and full reporting of outcomes
☐	☒	Estimates of effect sizes (e.g. Cohen's *d*, Pearson's *r*), indicating how they were calculated

Our web collection on statistics for biologists contains articles on many of the points above.

Software and code

Policy information about availability of computer code

Data collection	Custom Code: Investigational device firmware to capture multimodal sensor data Commercial Code: Philips Respironics Alice 6 LDx Diagnostic Sleep System to capture PSG data, 3T Siemens Vida system to capture MRI data Open-Source Code: Device and PSG signal processing used open-source libraries Python 3.8.5, NumPy 1.21.6, SciPy 1.9.3, Pandas 1.5.2, Matplotlib 3.6.2, Seaborn 0.12.1, EMD 0.6.2, Heartpy 1.2.7, yasa 0.6.3, Impedance 1.4 Open-Source Code: CE MRI signal processing included Python 3.8.5 using openly available packages FSL 6.0.5.1, dcm2niix 1.0.20190902, and it included Matlab r2022b and Matlab libraries IVIM_lib and NIfTI_tools
Data analysis	Custom R version 4.2.1 code was written to implement backward elimination and bootstrapping derived measures described in Heinze, G., Wallisch, C. & Dunkler, D. Variable selection - A review and recommendations for the practicing statistician. Biom J 60, 431-449 (2018). Custom R version 4.2.1 code was written to reduce threshold regression models to linear regression models as described in Supplemental 2. R version 4.2.1 was used for all other data analysis using open-source libraries nlme 3.1-162, lmtest0.9-40, sjPlot 2.8.14 and effects 4.2-2.

For manuscripts utilizing custom algorithms or software that are central to the research but not yet described in published literature, software must be made available to editors and reviewers. We strongly encourage code deposition in a community repository (e.g. GitHub). See the Nature Portfolio guidelines for submitting code & software for further information.

Data

Policy information about availability of data

All manuscripts must include a data availability statement. This statement should provide the following information, where applicable:

- Accession codes, unique identifiers, or web links for publicly available datasets
- A description of any restrictions on data availability
- For clinical datasets or third party data, please ensure that the statement adheres to our policy

The human subject data supporting this study are available at DOI: https://doi.org/10.5281/zenodo.15059617. Access requires Institutional Review Board (IRB) approval and a completed Data User Agreement (DUA). A blank DUA can be found at https://tinyurl.com/appliedcognition-dua. To obtain access, please submit IRB approved use and completed DUA to the corresponding author or research@appliedcognition.com

Research involving human participants, their data, or biological material

Policy information about studies with human participants or human data. See also policy information about sex, gender (identity/presentation), and sexual orientation and race, ethnicity and racism.

Reporting on sex and gender	Participants self-reported their gender. Genetic determination of sex was not performed. The Benchmarking Study and Replication Study were designed to enroll equal numbers of female and male gender participants. In the Benchmarking Study, of the 30 participants that completed the data collection, 14 self-reported as female and 16 as male. In the Replication Study, of the 14 participants, 7 self-reported as female and 7 as male. Statistical models included gender, age, APOEe4 status, site and site-age interaction as potential confounders.
Reporting on race, ethnicity, or other socially relevant groupings	Race, ethnicity and other social groupings were not used as a factor within the analysis or conclusions.
Population characteristics	The Benchmarking Study enrolled 34 healthy participants 56-66 years of age. The Replication Study enrolled 14 healthy participants 49-63 years of age. In both studies, participants were excluded if they had cognitive impairment or clinical depression. Cognitive impairment was assessed using the Montreal Cognitive Assessment (MoCA, 28.1 +/- 1.2; range 26, 30) and depression was evaluated using the 15-item Geriatric Depression Scale (GDS, 0.7 +/- 1.1; range 0, 4). Participants with a self-reported history of diabetes, hypertension, coronary artery disease, pulmonary disease, neurological disease, depression or anxiety were also excluded from the either study as were participants planning travel to alternate time zones within two weeks of study participation. In the Benchmarking Study, of the 30 participants that completed the data collection, 8 were APOEe4 positive, and in the Replication Study, of the 14 participants, 5 were APOEe4 positive.
Recruitment	The Benchmarking Study was conducted in The Villages community. Participants were recruited using study flyers in public-facing locations in senior recreation and/or local medical centers, and by word-of-mouth referrals from residents. The Replication Study was conducted at the University of Washington and participants were recruited with email outreach and by word-of-mouth referrals from professional colleagues. Self-selection biases include family history of Alzheimer's disease and subjective memory concerns but these are not expected to have an impact on study findings. All participants underwent genetic testing for APOE status and blood biomarker analysis for the presence/absence of amyloid.
Ethics oversight	All studies were performed between October 2022 – June 2023 were reviewed and approved by University of Florida Institutional Review Board (IRB No. 202201364, Benchmarking Study) and Western Institutional Review Board (IRB No. 20225818, Replication Study)

Note that full information on the approval of the study protocol must also be provided in the manuscript.

Field-specific reporting

Please select the one below that is the best fit for your research. If you are not sure, read the appropriate sections before making your selection.

☒ Life sciences ☐ Behavioural & social sciences ☐ Ecological, evolutionary & environmental sciences

For a reference copy of the document with all sections, see nature.com/documents/nr-reporting-summary-flat.pdf

Life sciences study design

All studies must disclose on these points even when the disclosure is negative.

Sample size	Sample size calculations for the Benchmarking Study were based on the primary objectives of the study to establish a relationship between sleep-/wake-associated measurements between the investigational device and contrast-enhanced MRI (CE-MRI). The study was powered to show a difference in contrast neuroimaging of glymphatic function in the overnight and morning study periods, and to show a correlation in those differences with observed changes in device measurements. Based on prior overnight MRI measurements comparable to the neuroimaging in this study we expect a within subject Cohen's d of 0.5 to 0.7. Using d = 0.6, setting alpha = 0.05 and beta = 0.8 givens N = 25. In addition, to detect a low-to-moderate correlation r (r=0.5) between the device measurements and the MRI overnight changes of glymphatic function using a two-sided test, 5% significance level test (α=0.05) with power 80% power (β=0.2), requires a sample size of N=29.

	Assuming a 20% attrition between the first and second Study Visit, using N = 36 was used to power the study. Sample size calculations for the Replication study were similar but used alpha = 0.2 and beta = 0.8 that gave N = 15.
Data exclusions	A Consolidated Standards of Reporting Trials (CONSORT) diagram for the Benchmarking Study and Replication Study is provided. Within the Benchmarking Study, the first three participants were removed from analysis because of a sensor position change in the investigational device. One participant was unable to complete the first MRI session and withdrew from the study. Of the remaining 30 participants (61.9 +/- 2.6 years of age; 15 female, 15 male) that completed the Benchmarking Study, five overnight sleep studies and eight overnight wake studies failed data quality control due to excessive artifacts in the recordings, leaving 25 sleep studies and 22 wake studies in the Benchmarking Study device, PSG and MRI data. All participants enrolled in the Replication Study (55.6 +/- 4.6 years of age; 7 female, 7 male) completed the protocol. All overnight sleep data were usable, but three overnight wake studies were removed, two because of excessive artifact and one because of non-compliance with the wake protocol.
Replication	Individual participant protocol interventions/experiments in both the Benchmarking Study and the Replication Study were performed only once, not replicated.
Randomization	The Benchmarking Study and Replication Study were randomized cross-over trials where participants wearing the investigational device were subjected to one night of natural sleep and one night spent awake, separated by two or more weeks. The sleep/wake visit assignment was randomized. Participants self-reported as healthy and met strict inclusion/exclusion criteria thereby controlling for disease-related covariates. Statistical models included gender, age, APOEe4 status, site and site-age interaction to control for remaining covariates.
Blinding	Study site investigators and participants could not be blinded to participant allocation to sleep or wake. Their knowledge to participant allocation was not deemed to impact the acquired device physiologic, glymphatic and MRI imaging data. Investigators involved in the MRI image processing, Phillips EEG data processing and device data processing were blinded to group allocation.

Reporting for specific materials, systems and methods

We require information from authors about some types of materials, experimental systems and methods used in many studies. Here, indicate whether each material, system or method listed is relevant to your study. If you are not sure if a list item applies to your research, read the appropriate section before selecting a response.

Materials & experimental systems

n/a	Involved in the study	
☒	☐	Antibodies
☒	☐	Eukaryotic cell lines
☒	☐	Palaeontology and archaeology
☒	☐	Animals and other organisms
☐	☒	Clinical data
☒	☐	Dual use research of concern
☒	☐	Plants

Methods

n/a	Involved in the study	
☒	☐	ChIP-seq
☒	☐	Flow cytometry
☐	☒	MRI-based neuroimaging

Clinical data

Policy information about clinical studies

All manuscripts should comply with the ICMJE guidelines for publication of clinical research and a completed CONSORT checklist must be included with all submissions.

Clinical trial registration	NCT06060054, NCT06222385
Study protocol	The Replication Study can be found at ClinicalTrials.gov under clinical trial registration NCT06060054. The Benchmarking Study has been submitted to ClinicalTrials.gov and awaiting a clinical trial registration identifier.
Data collection	All studies were performed between October 2022 – June 2023, were reviewed and approved by University of Florida Institutional Review Board (IRB No. 202201364, Benchmarking Study) and Western Institutional Review Board (IRB No. 20225818, Replication Study). The Benchmarking Study was conducted in The Villages, an active-lifestyle senior living community in Central Florida where the University of Florida maintains a satellite academic research Center – The University of Florida Health Precision Research Center. The Replication Study was conducted at the University of Washington.
Outcomes	The Benchmarking Study primary outcome was confirming the effect of sleep state on device-measured glymphatic function and that those measures faithfully reflect glymphatic function measured by contrast enhanced MRI. Secondary outcomes were confirming the associations between device measure of glymphatic function and sleep stages, heart rate, and EEG spectral band power. The Replication Study primary outcome was confirming the effect of sleep state on device-measured glymphatic function, and secondary outcomes confirming the associations between those measures and sleep stages, heart rate, and EEG spectral band power.

Magnetic resonance imaging

Experimental design

Design type	Not applicable
Design specifications	Pre-contrast image acquisition followed by 10-minute and 240-minute post-contrast image acquisition
Behavioral performance measures	Not applicable. Pre and post contrast signal intensities were measured using regions of interest.

Acquisition

Imaging type(s)	Structural (Gadolinium-enhanced steady state imaging)
Field strength	3
Sequence & imaging parameters	We performed a 3D T1-weighted magnetization-prepared rapid acquisition with gradient echo (MPRAGE) with TR/TI/TE = 2300/900/2 ms, resolution = 1x1x1 mm^3 , field-of-view = 256x256x208 mm^3 , total acquisition time = 5:12
Area of acquisition	Whole brain

Diffusion MRI ☐ Used ☒ Not used

Preprocessing

Preprocessing software	dcm2niiX version v1.0.20211006, FSL v6.0
Normalization	Per subject, the two post-contrast T1 images were registered linearly to the pre-contrast T1 image. The pre-contrast T1 were normalized using non-linear transformations in FSL, specifically using FNIRT to a 2mm-MNI space template. The same non-linear transformation (warp) was applied to the post-contrast image after they were registered to the pre-contrast T1 image to ensure that all images were in the final 2mm MNI space.
Normalization template	MNI152_T1_2mm.nii.gz in FSL v6.0
Noise and artifact removal	Not applicable.
Volume censoring	Not applicable. However, if participant motion was observed in the form of blurring, ringing-like artifact, the participant was rescanned immediately.

Statistical modeling & inference

Model type and settings	Not applicable. Only pre- and post-contrast MRI signal intensities were recorded.
Effect(s) tested	Not applicable. See below for models and analyses.

Specify type of analysis: ☐ Whole brain ☒ ROI-based ☐ Both

Anatomical location(s)	The pre-contrast image was bias-corrected, and segmented into gray and white matter, and CSF. The segmentations were transformed and standardized to the same 2mm MNI space template using the non-linear transformation described above. Voxels were assigned as gray matter, white matter, or CSF if the corresponding tissue type was identified with at least 75% probability using FAST. Voxels were also assigned to sub-cortical structures using FIRST in FSL. Frontal, parietal, temporal, and occipital lobes were identified using the MNI Structural Atlas in FSL. Corresponding lobar gray and white matter masks were estimated by multiplying the lobar masks with the whole-brain gray matter mask and whole brain white matter masks. All sub-cortical structures were subtracted from the gray matter mask using the segmentation output of FIRST to ensure that the lobar gray matter masks only included the cortex. The ventricular mask was estimated by multiplying the CSF mask with the template ventricular mask in MNI space in FSL. To identify and segment the ICA, the registered and normalized pre- and 10-minute post contrast images were opened and superimposed in FSLeyes. Starting from an axial-section at the level of the optic nerve, slices were manually checked in the inferior-superior direction for a slice location where the internal carotid arteries were visible (between the petrous and clinoid segments) and before they bent to form the Circle of Willis. The voxel selection was based on the immediate 10-minute post contrast image showing the highest contrast enhancement in the arteries bilaterally, relative to the surrounding tissue.
Statistic type for inference (See Eklund et al. 2016)	Mean signal intensity in each ROI was recorded for analyses below.

Correction

See analyses below.

Models & analysis

n/a | Involved in the study
☒ ☐ Functional and/or effective connectivity
☒ ☐ Graph analysis
☐ ☒ Multivariate modeling or predictive analysis

Multivariate modeling and predictive analysis

Contrast-enhanced MRI of sleep-related glymphatic function was analyzed using a random intercept linear mixed effect model (R, lme in the lmne package). Glymphatic function was defined by measuring brain parenchymal contrast enhancement, the % change in T1-weighted signal intensity between 10-240 min post-GBCA injection (100% * (T240-T10)/T0) at each of eight regions of interest (ROIs): frontal cortical gray and white matter, parietal cortical gray and white matter, temporal cortical gray and white matter, and occipital gray and white matter. Only sleep visits were analyzed leading to a one level of grouping, the eight ROIs, for the participant sleep visit. All models included regressors in the mixed model for the T10-T240 change in blood signal within the internal carotid artery, and the T10-T240 change in CSF signal within the cerebral lateral ventricles to compensate for the influence of vascular and CSF contrast on parenchymal enhancement. Potentially confounding biological variables age, gender, and APOE ε4 status were also included in all models.